THESIS FOR THE DEGREE OF DOCTOR OF PHILOSOPHY

The Functional Microstructure of Al/AlO_x/Al Tunnel Junctions

SAMIRA NIK

Department of Applied Physics
CHALMERS UNIVERSITY OF TECHNOLOGY
Göteborg, Sweden 2013

The Functional Microstructure of $Al/AlO_x/Al$ Tunnel Junctions
Samira Nik
ISBN 978-91-7385-907-3

Doktorsavhandlingar vid Chalmers tekniska högskola
Ny serie nr 3588
ISSN 0346-718X

Department of Applied Physics
Chalmers University of Technology
SE-412 96 Göteborg
Sweden
Telephone + 46 (0) 31-772 1000

Cover: The upper figure, a scanning electron microscopy (SEM) image showing an overview of an $Al/AlO_x/Al$ tunnel junction. The figure to the left, a cross-sectional bright field transmission electron microscopy (BF-TEM) view of the junction. The figure to the right, a plan-view BF-TEM image showing an abnormally large grain in an Al thin film.

Chalmers Reproservice
Göteborg Sweden 2013

The Functional Microstructure of Al/AlO_x/Al Tunnel Junctions
Samira Nik
Department of Applied Physics
Chalmers University of Technology

Abstract

Josephson junction as a novel superconducting electronic component plays an important role in most small-scale superconducting systems. Particularly the Al/AlO_x/Al tunnel junction, a high-performance junction made with a well-established microfabrication technology, is widely used as a building block of many quantum circuits. However, the performance of these devices is limited by unwanted coupling between the device and environment, decoherence and different types of noise. The origin of noise and decoherence in superconducting devices containing tunnel junctions has attracted a lot of attention but there is no concurrency on the subject. Many investigations have been carried out using electrical measurements and computer simulations. However, very little information is available about the detailed microstructure of the tunnel junctions and therefore the physical origin of noise is still unknown.

Consequently, it is important to understand the microscopic nature of the tunnel junctions and correlate the structural information to electrically measured characteristics of the devices such as noise, RC (resistance capacity) products, sub gap current and decoherence times.

The present work concerns the functional nanostructure of Al/AlO_x/Al tunnel junctions and how it develops during the fabrication of the tunnel junctions. The unique aspect of this work is the ability to directly correlate the local structure to properties on the nanoscale and the close collaboration and interplay between the research groups fabricating the junctions, characterising the properties of the junctions and performing high resolution imaging and spectroscopy of the same individual junctions. The functional microstructure, i.e. the microstructural constituents that determine the properties, has been identified. Information is provided about the fine scale microstructure of the individual patterned and electrically characterised nanodevices. An important aspect is the control of the evolution of the microstructure in order to control the properties on a local scale and not only the average structure. Information about how to obtain a more uniform morphology and internal structure of the tunnel barriers is deduced from the studies.

The high spatial resolution microstructural investigations have been performed using imaging and spectroscopy by scanning electron and transmission electron microscopy.

Keywords: Microstructure, Superconducting Tunnel Junctions, AlO_x Tunnel Barriers, Interfaces, Transmission Electron Microscopy, Imaging, Spectroscopy, Grain Growth.

To my beloved parents

There is something in my heart
Like a grove of light
Like an early morning dream
And I am so anxious
That I wish to run to the end of the filed
To go to the top of the mountain

Far far away there is a sound
Calling for me

Sohrab Sepehri

Perisan Painter and Poet
1928-1980

PREFACE

The research presented in this doctoral thesis has been carried out at the Microscopy and Microanalysis group and at the Eva Olsson group at the Department of Applied Physics, Chalmers University of Technology, Göteobrg, Sweden, 2008-2013, under the supervision of Prof. Eva Olsson. This work has been a part of collaboration with Dr. Tine Greibe, Philip Krantz and Prof. Per Delsing at the Quantum Device Physics Laboratory, Department of Microelectronics and Nanoscience.

List of Appended Papers

I. H. Pettersson, S. Nik, J. Weidow and E. Olsson, "*A method for producing site specific TEM specimens from low contrast materials with nanometer precision*", Microsc. Microanal. **19**, 73-78 (2013)

II. L.J. Zeng, T. Greibe, S. Nik, C. M. Wilson, P. Delsing and E. Olsson, "*Interaction layer at the interface between Al films and SiO2 substrates of Al/AlOx/Al Josephson tunnel junctions*", J. Appl. Phys. 113, 143905-143909 (2013)

III. S. Nik, P. Krantz, L.J. Zeng, H. Pettersson, T. Greibe, P. Delsing and E. Olsson, "*The control and role of Al grain size for the properties of Al/AlOx/Al tunnel junctions*", submitted for publication

IV. S. Nik, T. Greibe, L.J. Zeng, P. Kranz, C. Wilson, P. Delsing and E. Olsson, "*Atomic structure of patterned nanoscale Al/AlOx/Al tunnel junctions*", in manuscript

V. L. J. Zeng, S. Nik, T. Greibe, C. M. Wilson, P. Delsing and E. Olsson, "*Direct observation of thickness of AlOx barrier in Al/AlOx/Al Josephson junctions*", in manuscript

TABLE OF CONTENTS

Chapter 1

Introduction

This chapter gives a brief introduction to the field of this study and the aim of it.

1.1 Background

The achievements of quantum information theory in the 1990's opened up a new horizon in the field of information technology. The discovery of the fact that quantum algorithms can run exponentially faster than their classical compeers encouraged scientists to picture building unique types of information processors where the quantum mechanical principles rule instead of classical physics used so far [1-2]. However, constructing such computers is entangled with a dreadful scientific and technological challenge. Although the quantum bits (qubits) should be firmly inter-coupled by gates to carry out quantum computation, they must at the same time be fully decoupled from external influences, with the exception of the write, control and readout phases when information must flow in and out of the machine deliberately. The classical bits of an ordinary computer do not face such a problem since each of them follows highly irreversible dynamics that damp the environment noise [2].

Among many proposals for physical realization of quantum computers, the most promising approach was offered by nanoelectric systems. It is relatively straightforward to scale these systems to large number of qubits and they integrate quite well into electronic circuits [1]. In particular superconducting qubits are outstanding candidates for quantum processing. The large electromagnetic cross-sections of these qubits allow them to easily couple with each other in complex topologies through simple electrical elements like indicators, capacitors and transmission lines. Superconductive qubits are conveniently scalable because the complex circuits can be built up using well-established integrated circuit

microfabrication technology. An essential element of these kinds of qubits is the Josephson junction, which has a sandwich structure consisting of two superconducting thin films separated by a thin insulating layer [2-5]. The Josephson junction is a novel superconducting electronic device used as a core element in most small-scale superconducting systems and has a variety of applicants. For instance Superconducting Quantum Interfacing Devices (SQUIDs) are based on Josephson junctions and they are used as magnetometers, gradiometers, low-frequency and microwave amplifiers and also in applications including reading out superconducting qubits, magnetocardiography, cosmology, non-destructive evaluation and Magnetic Resonance Imaging (MRI) in microtesla fields [6-8].

As the performance standards for devices containing Josephson junctions such as quantum bits, become stricter the properties of the oxide barrier become more vital. Since the size of these devices get smaller and likewise the oxide barrier becomes thinner, the atomic-scale defects may lead to an unwanted coupling between the environment and the qubits, known as decoherence [9-11]. Decoherence time is a crucial parameter in quantum computing devices. In order to perform quantum computation the whole system should stay coherent for a sufficiently long time, which means the system should have a weak coupling to the environment. Therefore, decoherence is a major limiting factor in the performance of a practical quantum computer and a detailed study of decoherence time and its origin would provide substantial information for designing solid-state quantum circuits [2,4], [12-15].

There are different sources of decoherence and noise in an electronic system. For example it is thought that the spontaneous photon emission to the electromagnetic environment is the main decoherence source. However, in a probe junction quasiparticle tunnelling through the junction is considered as the main decoherence source [17]. On the other hand, dielectric loss both in the tunnel barrier and the wiring crossover insulator is a confining issue for the performance of qubits made of superconducting Josephson junctions. Therefore, the material component of the qubit itself can be the origin of decoherence and optimization of the materials used in the junction, for example in the tunnel barrier, can improve the qubit performance [4,12]. Many groups have applied different fabrication methods and materials in order to optimise the superconducting devices made of Josephson junctions and it is generally considered that material properties are an influential limiting factor in the strive for longer coherence times [2], [9-10], [16-22].

Consequently, a systematic study of the effect of material and fabrication parameters on the microstructure of superconducting devices, especially Josephson junctions, as building blocks of these systems, will provide valuable information about the possible sources of decoherence and noise.

1.2 Aim of this work

The present work concerns the characteristics and atomic structure of $Al/AlO_x/Al$ tunnel junctions. We aim to elaborate an understanding of microscopic characteristics that determines the junction properties and also to identify the features that give rise to noise in tunnel junctions. As mentioned in section 1.1 the origin of noise and decoherence in qubits containing tunnel junctions has attracted a lot of attention but

there is no concurrency on this issue. Many investigations on this matter have been carried out using electrical measurements and computer simulations. However, very little information is available about the microstructure of tunnel junctions and therefore the possible physical origin of noise is still unknown. Accordingly, it is important to understand the microscopic nature of the tunnel junctions and to correlate the structural information with electrically measured characteristics of the devices. Using the state-of-the-art instrumentation for making nanodevices as well as for electrical and structural characterisation, we studied the effect of different fabrication parameters like oxidation process parameters, choice of substrate material and also substrate temperature on the microstructure of $Al/AlO_x/Al$ tunnel barriers. The microstructural investigations have been performed using scanning electron microscopy (SEM) and transmission electron microscopy (TEM).

Chapter 2

Basic Quantum Mechanical Concepts For Superconducting Devices

This chapter provides a brief introduction to the basic quantum mechanical concepts needed to understand the function and performance of the superconducting devices investigated in this work.

2.1 Superconductivity

In 1911, Kamerlingh Onnes discovered the phenomenon of superconductivity [23]. He found out that below a critical temperature (T_c) the resistance of mercury dropped to zero and he called this new state of electrical properties *superconducting state*. Later on other superconductors like tin, lead, tungsten, niobium and aluminum have been identified and their critical temperatures cover a range as low as 0.01 K for tungsten to as high as 9.3 K for niobium.

Two years later Onnes discovered that a superconducting sample could carry a "threshold value" of current density before it reverts to its normal state. This value is known as the *critical current density,* J_c and it is dependent on the temperature: J_c increases as the temperature of the superconductor is lowered. He also figured out that applying a strong magnetic field can destroy the superconducting effect. This *critical field,* H_c, is temperature dependence as well. Another interesting fact about superconductors is that for low magnetic fields, a superconductor expels the flux instead of conserving it as a perfect conductor would (the Meissner effect) and therefore a superconductor can be a perfect diamagnet [24-25].

In order to reach effective engineering applications for these materials, a decent understanding of superconductivity is essential and thus different models for

superconductivity have been proposed. Two of the models that are used extensively are the *classical model of superconductivity* and the *macroscopic quantum model (MQM)*. The first model combines the zero resistance and perfect diamagnetism of superconductors with electromagnetic constitutive relations known as *London* equations (1935). This powerful model makes it possible to calculate and estimate the relevant parameters of a superconducting system, like superconducting current density and magnetic penetration depth.

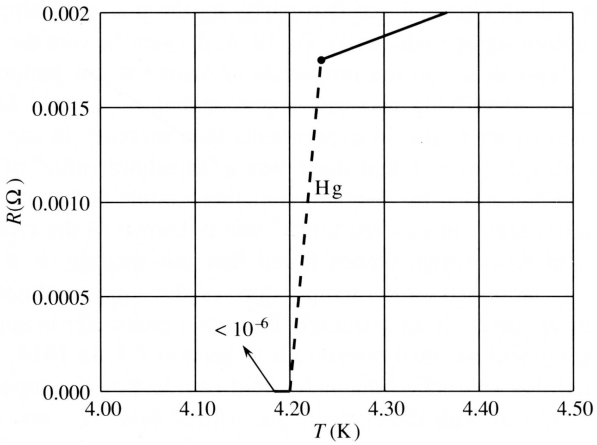

Figure 2.1. This plot shows the original resistance versus temperature curve reported by Kamerlingh Onnes to announce the discovery of superconductivity in mercury [25].

However, this model is based on experiments and is not derived from any microscopic mechanism within the material. The MQM model is based on the superconductivity model proposed by *Ginzburg* and *Landau* (GL theory, 1950), where they conjugate the electromagnetic and quantum mechanical properties of the superconductor, as well as its thermodynamic properties. This model comprehends the results from the classical model and also explains other properties of superconductors, which are important in applications like the study of Josephson junctions [25].

Despite their efficiency, these two models do not illustrate how superconductivity occurs. This issue can be described by the microscopic theory proposed by *Bardeen*, *Cooper* and *Schrieffer* (BCS theory) in 1957 [26]. The essence of the BCS theory is that the electrons that carried lossy currents in the metallic or normal state, couple together in the superconducting state and appear as a pair called Cooper pairs. These Cooper pairs carry the lossless super-currents and provide the perfect condition in the material. The density of Cooper pairs in a material depends on temperature; the lower the temperature, the more Cooper pairs are put together out of the normal state electrons. Therefore, it is anticipated that the strength of superconductivity increases at lower temperatures.

According to BCS theory, the electrons in a Cooper pair are bound with an energy 2Δ that is usually referred as the *energy gap* of the superconductor. Hence, in order to change the densities of normal electrons and Cooper pairs in a superconductor, at

least an energy in the order of 2Δ should be applied to split the Cooper pairs into two unbound electrons [25].

2.2 Tunneling

One of the essential ideas of quantum mechanics is the wave-particle duality of nature [25]. According to classical physics all macroscopic phenomena are divided in two classes; *elementary objects: particles*, which follow the laws of Newtonian mechanics and *wave fields*, which obey Maxwell's equations. In other words, every elementary object is either a particle or a wave field. But in quantum mechanics, these concepts have changed their character. Waves and particles are not classes of objects themselves. Instead, they are two distinct modes of behaviour that are shared by all classes of objects. Therefore, every object can behave like a particle and like a wave [27]. The wave like propagation of the electrons can be described by *wave functions (Y)* , which are themselves functions of both position and time:

$$\Psi = \Psi(\mathbf{r},t) \qquad (2.1.1)$$

The simplest wave function can be shown as a plane wave of the form

$$\Psi(\mathbf{r},t) = A\exp[i(\mathbf{k}\,\mathbf{r} - \omega t)] \quad (2.1.2)$$

Where **k** is a wave vector associated with the wave, and w is the wave frequency. These two properties characterize the state of the object from the wave point of view. Quantum mechanics hypothesizes that the two characteristics *particle-like* properties of each object, energy (ε) and momentum (**p**), are simply proportional to its two characteristics *wave-like* properties, frequency and wave vector [27].

Therefore we have:

$$\varepsilon = \hbar\omega \qquad \mathbf{p} = \hbar\mathbf{k}$$

where $\hbar$ is Planck's constant. These relations can be referred as the Planck-Einstein-de Broglie relations in honour of their discoverers and they are believed to be valid for all elementary objects of nature [27].

The concept of tunneling is a direct consequence of quantum mechanics. Imagine a piece of metal with its surface coated with a very thin layer of an insulator. If another piece of metal will be placed on top of it, a sandwich structure will be formed, known as tunnel junction (Figure2.2). Classically, driving a dc current through the junction would be impossible since the electrons would not able to pass through the insulating layer. However, according to quantum mechanics the electron wave function can stretch across the barrier and the probability of having an electron passing through, or *tunneling* through, the barrier increases by making the insulator layer very thin. Therefore, when many carriers are available for tunneling, like in a metal, and the insulator is very thin (~10 Å) an observable dc current can pass through the structure [25].

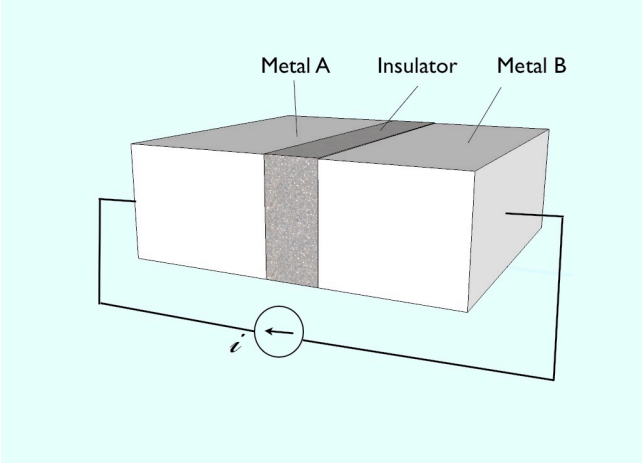

Figure 2.2 Schematic of a tunnel junction. For the sake of clarity the insulating layer is shown as a tick layer in this sketch but it is a very thin layer in reality.

2.3 Tunnel Junctions

Electron tunneling between a normal metal and a superconductor, separated by an insolating layer, was experimentally observed by *Giaever* in 1960. These tunnel junctions are classified as superconducting-insulator-normal (SIN) junctions and as it is shown in Figure 2.3 when such a junction is cooled below T_c, the resistance of the structure increases with a range of voltage. This effect can be explained by BCS theory. As it was mentioned in section 2.1, Cooper pairs are bound with an energy of 2Δ and if a pair is split up each electron will have an energy of at least Δ. This means that normal electrons (not paired) in a superconductor have an energy at least Δ over the energy they would have in the normal state of the material.

Since Cooper pairs do not exist under normal conditions in a metal, the carriers must be normal electrons when a dc current passes through an SIN junction. The conclusion is that a normal electron can tunnel from the metal into the superconductor if its energy is increased by an amount Δ. Therefore, no current can pass until a voltage of at least Δ/e biases the junction, where e is the charge of an electron (Figure 2.3) [25].

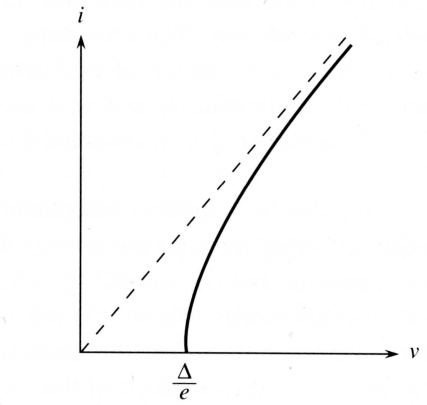

Figure 2.3 The *i-v* curve for a SIN tunnel junction, where the dotted line is the characteristics for temperatures above T_c and the solid line for temperatures below T_c [25].

Considering a junction made of two identical superconductors separated by an insulating layer (SIS), no normal electrons are available to carry the current as in the pervious case. Thus, the Cooper pairs should break into electrons that can tunnel through the insulating layer. The *i-v* characteristic of this tunneling is expected to be similar to the one for SIN junctions where the minimum needed voltage would be $2\Delta/e$, and this behaviour is indeed observed.

Here, tunneling of the Cooper pairs as current carriers was omitted because before 1962 the general belief was that this kind of tunneling does not occur with a high enough frequency to be statistically adequate. But in 1962 Brian Josephson discovered that a Cooper pair could tunnel through the barrier with the same probability as that for a single electron [28]. The reason is that tunneling of a Cooper pair is a coherent process and should not be treated as two electron wave functions leaking across the insulating layer. In fact, what tunnels from one superconductor to another is the *microscopic wave function*. In honor of his discovery, the SIS junctions are called Josephson junctions [25].

Figure 2.4 shows the *i-v* curve for a Josephson junction. The two branches, which are similar to the ones observed in an SIN junction *i-v* characteristic, represent tunneling of the normal electrons. The current at zero voltage is the outcome of the Cooper pair tunneling and it is known as the *Josephson current*. The range of currents that can flow by Josephson tunneling is depicted with the curve at zero voltage. The behaviour of these currents, which can pass through the insulating layer with no voltage, is essentially important for many practical applications.

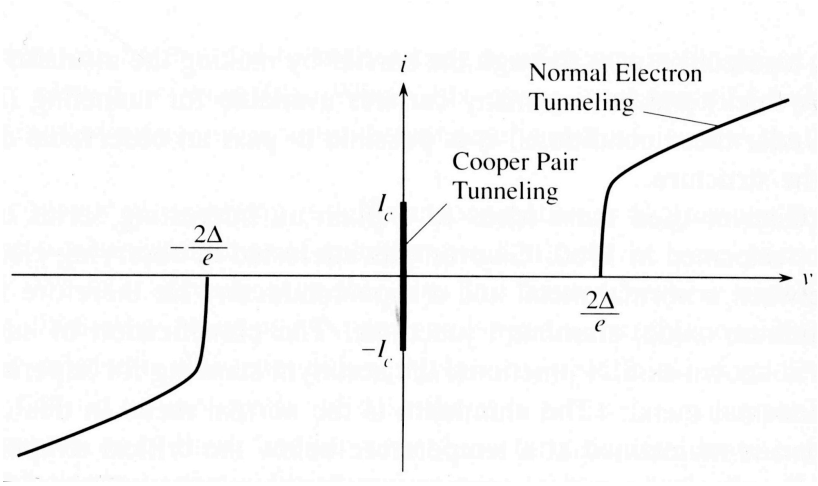

Figure 2.4 The *i-v* curve for a Josephson junction. The current at zero voltage represents the Josephson current [25].

Due to Josephson tunneling, applying a dc current to the junction do not cause a voltage drop over it. Even so, it is a limited amount of current that the tunneling Cooper pairs can carry and applying too much current demolishes the Josephson effect and thus normal electrons would carry the current. The *Josephson critical current density* J_c defines the maximum dc current density that can pass through the junction at zero voltage. Applying a current that exceeds J_c will develop a voltage

drop through the junction, which means that increasing the dc current makes it possible to switch from a zero voltage to a finite voltage stage, granting the development of a binary digital logic (qubits). The digital technology based on Josephson junctions requires much less energy compared to semiconductors and they also generate less heat and can thus be packed more densely [25].

In general the novel properties of Josephson junctions, consequences of coherent tunneling, make them suitable for many practical applications such as SQUIDs and qubis. But the optimal performance of these devices is affected by noise and decoherence. The following section provides more information about noise in superconducting devices.

2.4 Noise in superconducting devices

A random fluctuation in an electronic signal or an unwanted distribution of a signal in electronic devices is referred to as noise. There are different possible sources of noise; some of them arise from the nature of the material and some from the connection between the device and the environment.

2.4.1 Energy decay

Energy loss is an important source of decoherence in superconducting devices. For instance, in a qubit the energy loss causes the |1> state to decay to the |0> state at a rate $1/T_1$, where T_1 is the decay time. It is believed that this energy decay happens due to radiation of the qubit energy to the leads attached to the device, usually called the environment. Another energy loss mechanism comes from trapped vortices in the superconducting ground plane and depends on the geometry of the device and choice of material. One of the most important energy loss mechanisms is dissipation from Two-Level States (TLS) in dielectric materials. The density of TLS is large in amorphous materials, because TLS are presumed to arise from the random bonding of atoms in amorphous materials and they are modelled as atoms tunneling between two atomic configurations or positions. According to these mechanisms radiation effects limit the decay time, T1, and dielectric loss and it can be improved by fabricating smaller size devices that causes less radiation and surface losses. In addition, replacing the amorphous dielectric with a crystalline dielectric will reduces the density of TLS and therefore improves the performance of the device. However, epitaxial growth of an insolating layer with a good interface quality demands a considerable materials challenge [3], [29-30].

2.4.2 Dephasing

Dephasing is noise in the phase between two qubit states and it is calculated from fluctuations in the qubit energy. These energy fluctuations arise from noise in qubit parameters, where they fluctuate with a strong low frequency component (*1/f* noise). The most important fluctuating components are charge, flux, and junction critical current. For example, the background charges in the substrate can couple with the device and dephase the quantum state (*charge noise*). The *1/f flux* noise is the

dominant dephasing mechanism and its origin have been an open question for more than 20 years [3], [31-34].

These investigations and definitions lead us to the fact that both material properties and fabrication methods can have significant effect on the quality of the superconducting devices. Therefore, a systematic study of a sequence of samples fabricated with specific materials and parameters can provide vital information about the source of noise and decoherence.

Chapter 3

Grain Growth in Thin Films

Grain growth often occurs during or after deposition of thin films and causes an increase in the average grain size of the film. After briefly explaining the film formation, the mechanisms and reasons behind grain growth in thin films will be described in this chapter.

3.1 Thin film formation

As a thin film is fabricated by an evaporation technique, small nuclei will start to form on the substrate soon after deposition begins. When the nuclei reach a specific size called the critical size, they can become stable and start to grow and form islands. The individual islands grow in three dimensions and start to coalescence and form a continuous network. Further deposition will fill the channels and voids in the network and results in a continuous film. However, the size of the formed crystallites depends on the critical size of the nuclei, which in turn depends on the substrate temperature and the deposition rate. High substrate temperature results in the formation of larger nuclei but also a fewer number of them. Therefore, making a continuous film will require longer times at elevated temperatures. On the other hand, lower deposition rates result in the formation of smaller islands. Thus high substrate temperatures and low deposition rates will result in a large grained polycrystalline film or even a monocrystal, while low substrate temperatures and high depositions rate give rise to a fine-grained polycrystalline film [35].

3. 2 Grain Boundary Groove

When a metal thin film is hot enough to allow the atomic migration, a thermal groove will form at the intersection of the grain boundary and the free surface of the film (Fig. 3.1). This process is motivated by the desire of the grain boundary to shrink in

order to reduce its area and thus the free energy. The dominant transport process for groove development is surface diffusion, which could redistribute matter to allow a groove to move or grow deeper [36].

What makes the grooves interesting is their effect on the mobility of the grain boundaries and hence on the grain growth. Mullins explained the process of groove growth and motion in a detailed model that will be briefly explained here.

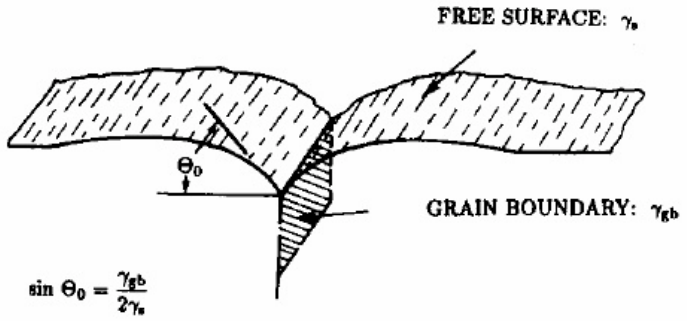

Fig.3.1 The profile of a grain boundary groove [37]

In order to understand how a grain boundary get trapped by a groove, Mullins considered the groove as a rigid V-notch that remains fixed regardless of changes in the associated boundary. As it is shown in Fig. 3.2 the associated grain boundary can seat in different positions. If the boundary is positioned between the lines perpendicular to the walls of the notch, marketed with *a* and *b*, it will be anchored to the notch as it can only escape by elongation. Diversely, when a boundary makes an angle larger than θ_0 with the line perpendicular to the top surface (L) it will escape from the notch since it may accordingly shrink. It is important to know that the impact of the notch to trap a grain boundary depends on Θ_0 but not its depth [36].

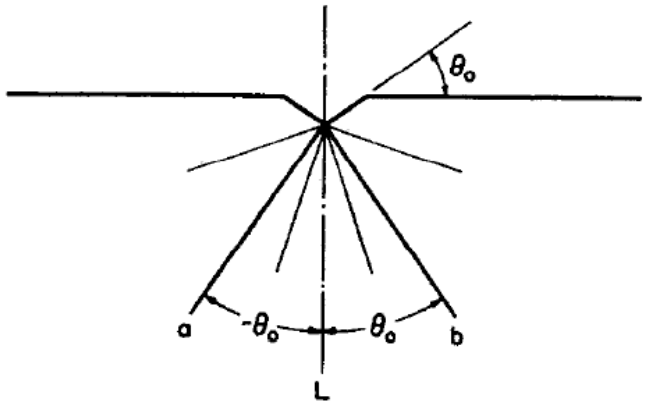

Fig. 3.2 Sketch of a grain boundary that anchors at a notch [36]

Another interesting case modelled by Mullins is columnar grains whose boundaries have in-plane curvatures and intersect the free surfaces of the film along circular grooves. Considering the boundaries to be pinned at the surfaces (top and bottom) by these circular grooves, they are still free to migrate inside the film in order to

minimize their area and hence the total grain boundary energy. This minimization gives rise to a catenoid shape grain boundary shown in Fig. 3.3. In this catenoid shape, the net local driving force for grain boundary migration disappears because the in-plane curvature of the grain boundary is balanced by the out-of-plane curvature. The catenoid intersects the surface at an angle (θ) defined by the ratio of the film thickness a to the radius of the curvature r. For instance when $r \gg h$ the angle can be defined by $\theta \approx a/2r$. Merging the catenoid properties with the previous considerations of θ_0 Mullins concluded that a columnar grain with $\theta < \theta_0$ will be pinned to its grooves while it can escape and shrink if $\theta > \theta_0$ [36-37].

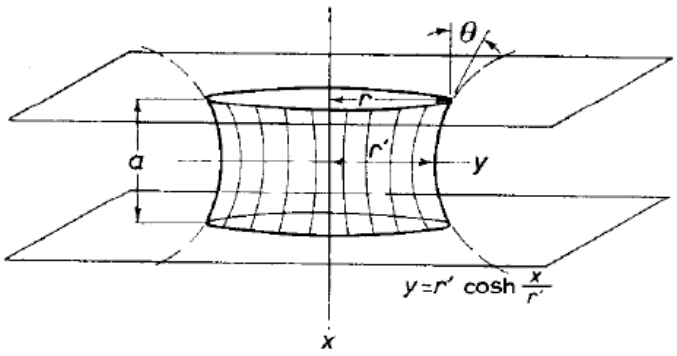

Fig. 3.3. Catenoid surface that spans between circular traces in parallel planes [36]

According to this model when two columnar grains in their equilibrium catenoid shapes have radii of $r_2 > r_1$, the larger grain is pinned to the groove while the smaller grain can escape and shrink (Fig. 3.4) [36]. This issue plays an important role in grain growth.

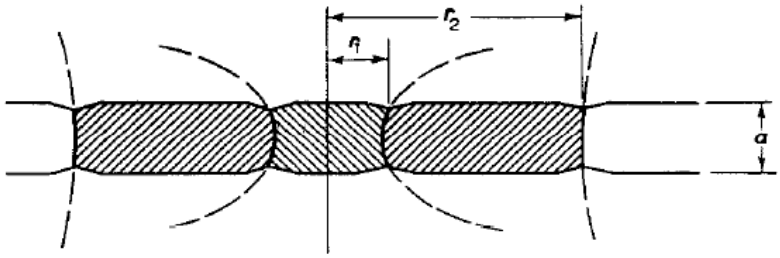

Fig. 4.3 Illustration of cross-sectional view of idealized grains in a thin film [36]

3. 3 Grain Growth

In polycrystalline thin films with columnar grains, the grains reach the thickness of the film in the direction normal to the film while their in-plane size can be much smaller or larger than the film thickness. This fact can be explained through *grain*

growth that happens when some grains grow in the matrix at the expense of other grains. The two modes of grain growth, normal and abnormal, will be explained here [38-39].

3. 3. 1 Normal Grain Growth

The theory of normal grain growth is based on minimization of the total energy of the system due to reduction of the energy associated with grain boundaries. In this mode of growth, some grains grow larger at the expense of other grains and the average grain size increase continuously. This grain size increment results in a reduction of the total grain boundary area and thus the energy associated with grain boundaries, which consequently lower the total energy of the film. In other words, the driving force for normal grain growth is lowering of the total energy associated with grain boundaries. It should be noted that in this model all boundaries are considered to have the same energy (γ_{gb}) [38], [40-41].
In the normal growth process the average grain size changes with time (t) as following

$$d^2 - {d_0}^2 = ct \qquad (3.1)$$

Where d is the average grain size, d_0 is the average grain size at $t = 0$ and c is a time independent, but strongly temperature dependant, element which may be modelled according to $c = c_0 \exp(-Q/kT)$. The change of average in-plane grain size from d_0 to d results in an energy change of

$$\Delta F_{gb} = \gamma_{gb}\left(\frac{2}{d_0} - \frac{2}{d}\right) \qquad (3.2)$$

The local motion of a grain boundary during growth has the in-plane velocity of v normal to the grain boundary

$$v = m\gamma_{gb}r \qquad (3.3)$$

Where m is the grain boundary mobility which has a temperature dependence of $m = m_0 exp(-Q/kT)$ and r is the mean in-plane curvature of the grain boundary [38]. According to the model suggested by Mullins, (Fig. 3) when a grain boundary extends through a film and have circular arcs of radii r at the surface, it will make an angle of $\theta = {a}/{2r}$ $(r \gg a)$ with the surface normal. Now considering a polycrystalline film where its grain boundaries appear as circular arcs on the surface, if $\theta = {a}/{2r} < \theta_0$ for every arc then all grain boundaries will be eternally pinned in their own thermal grooves. Therefore, the grain growth must stop when the radii of curvature of all boundaries exceed ${a}/{2\theta_0}$.

Following the discussion above one can assume that the average radii of boundaries curvature $(\bar{r})$ is related to the average grain diameter $(\bar{d})$ by $\bar{r} = \sigma\bar{D}$.
Consequently the rate of grain growth should decrease quickly when

$$\bar{d} = \bar{d}_{max} = \frac{\bar{r}_{max}}{\sigma} \cong \frac{a}{2\theta_0 \sigma} = \frac{3\gamma_{sf}}{\sigma \gamma_{gb}} a \qquad (3.4)$$

Due to the fact that σ, γ_{sf} and γ_{gb} are constant, the final grain size $\bar{d}_{max}$ should be proportional to the film thickness a and since $\gamma_{sf}/\gamma_{gb} \sim 2-3$ and $\sigma \sim 5$, the final grain size is roughly 1 or 2 times the film thickness. A more accurate approximation from Frost, et al suggested that the normal grain growth stops when the average grain diameter is almost 2.9 times the film thickness. This effect is known as the *Thickness effect* and has been proved experimentally [36-37].

As the normal grain growth occurs and the grain boundaries move, they leave some traces on the film surface, surface topography. In fact, the grain boundaries produce grooves in the places that they occupied earlier, and these appear as networks of lines on the film surface [36].
According to the experimental results and also computer simulations the grain size distribution of normal grain growth is mono-modal and the shape of the distribution curve does not change with time [37-38], [40-41].

3. 4. 2 Abnormal Grain Growth

As it was discussed in the previous section when the average grain size in thin films becomes two or three time the film thinness, the normal grain growth stalls. However, grain growth can continue after this stagnation by abnormal growth of a few grains. In fact, having grains larger than the film thickness indicates that the area of the free surface of the film is comparable to the area of the grain boundaries. If the free-surface energy varies sufficiently on the thin film, then the minimization of this energy becomes an influential driving force for the grain boundary migration. Mullins proposed that grains with different crystallographic orientations have various free-surface energies. Thus two grains in a thin film separated by a grain boundary have different free-surface energies, $\gamma_1 > \gamma_2$ (Fig. 3.5), which results in expansion of the grain with lower free- surface energy on the expense of the one with higher free-surface energy.

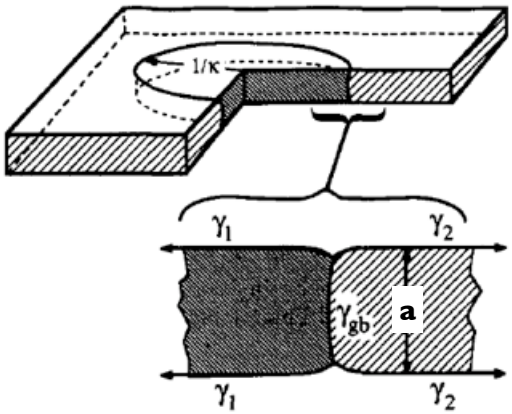

Fig 3.5 Schematics of neighbouring grains with different free-surface energies [39]

The driving force arising from the difference in free-surface energies can be expressed as

$$\Gamma = \frac{2\Delta\gamma}{a\gamma_{gb}} \tag{3.5}$$

Due to the fact that reducing the free-surface energy is the driving force for abnormal grain growth and also experimental results showing that grains with specific orientations have lower energies, the abnormally large grains might have the same orientation. For example in FCC metals, thin films deposited on an amorphous substrate grains with (111) orientation have the lowest free-surface energy. This implies that the abnormally big grains in such a thin film should all have (111) orientation [36, 42].

Chapter 4

Materials and Sample Fabrication

This chapter describes fabrication of the samples used in this work as well as choice of material and tuned parameters. All fabrication has been done in the Nanofabrication Laboratory at the Department of Microtechnology and Nanoscience (MC2), Chalmers University of Technology.

4.1 Materials

The samples studied in this thesis are made of evaporated aluminum (Al) thin films. Aluminum is extensively used in the field of engineered quantum systems, due to its superconducting properties, flexibility in fabrication, and its naturally growing oxide that can form at room temperature and has a proper thickness to be used as a tunnel barrier [43-46].

The samples were fabricated either as Josephson junctions with a specific pattern or as non-patterned junctions with three simple layers. In addition, samples with just a single layer of aluminum have been investigated.

Most of the samples were fabricated on silicon (Si) substrates with a 400 nm layer of silicon oxide (SiO_2), referred to as Si/SiO_2. Three other substrates that were used are Si with a native oxide of thickness of 2 nm, silicon nitride (Si_3N_4) and sapphire (Al_2O_3).

4.2 Sample Fabrication

The samples characterized in this thesis were fabricated using two-angle evaporation through a bilayer resist mask, where oxidation of Al takes place between the two evaporation steps, followed by lift-off of excess Al [47]. The features of the devices were defined using two different lithography techniques. First, large-scale patterns in the range of several millimeters, like contact pads, were defined by photolithography. In this technique the desired pattern is obtained by exposing UV light to a photoresist-

covered substrate, which is pressed against a glass mask containing the pattern. The procedure is completed by development in a chemical bath that removes regions that were not exposed to the light and transfers the pattern into the resist. This technique is quite simple but it has a limited resolution. Therefore, finer structures such as junctions with the size of a few hundred nanometers were defined by a more complex and expensive technique called Electron Beam Lithography (EBL). This method does not demand a pre-fabricated lithography mask. Instead, a computer-controlled electron beam move around and expose the resist according to the computer drawing. A development process similar to the one used for photolithography fulfills the procedure [48-49].

Different techniques can be used for deposition of metal films and in this work Physical Vapor Deposition (PVD) or namely evaporation was applied. Evaporation coating takes place in a high-vacuum chamber, where the source material is placed at the bottom and the substrate at the top. The source material can be heated in two ways, by passing a high electrical current through the holder (thermal heating) or by bombarding the material with an electron beam (e-beam heating). As the material reaches its evaporation temperature, atoms leave the source towards the chamber walls and the substrate and stick there.

The contact pads of the devices used in this work were made by evaporation deposition of a thin layer of titanium (5nm), as a sticking layer between substrate and gold, followed by deposition of 80 nm of gold and 5 nm of palladium that works as an adhesive layer between the photolithography pads and the aluminum e-beam pattern. The Josephson junctions were also created by an evaporation method called two-angle evaporation or shadow evaporation. The principle of this method is described schematically in Figure 4.1 The first step is to deposit a layer of Al on the substrate with an angle α. This layer that we recall as the bottom layer has the thickness of 15 nm in most of the samples and in a few cases it is 40 nm thick. The next step is forming a thin tunnel barrier of AlO_x by letting oxygen gas of controlled pressure (P_{ox}) into the chamber for a specific time (t_{Ox}) (Table 4.1). Thereafter, the oxygen gas is pumped out of the chamber and the second Al layer is deposited by an angle – α. This layer will be referred to as the top layer and has a thickness of 60 nm [48-50]. The detailed steps of the fabrication procedure can be found in Appendix A.

The majority of the samples are fabricated with no special heat treatment and only a few samples are made while the substrate was cooled down to -100 °C or -195 °C using liquid nitrogen.

Fabrication parameters			
Oxidation time, t_{ox} (min)	3	10	30
Oxidation pressure, P_{ox} (mbar)	0.01	0.1	1
Deposition rate	5-10 Å/s		
Deposition angles	+/- 28 °		

Table 4.1. Fabrication parameters

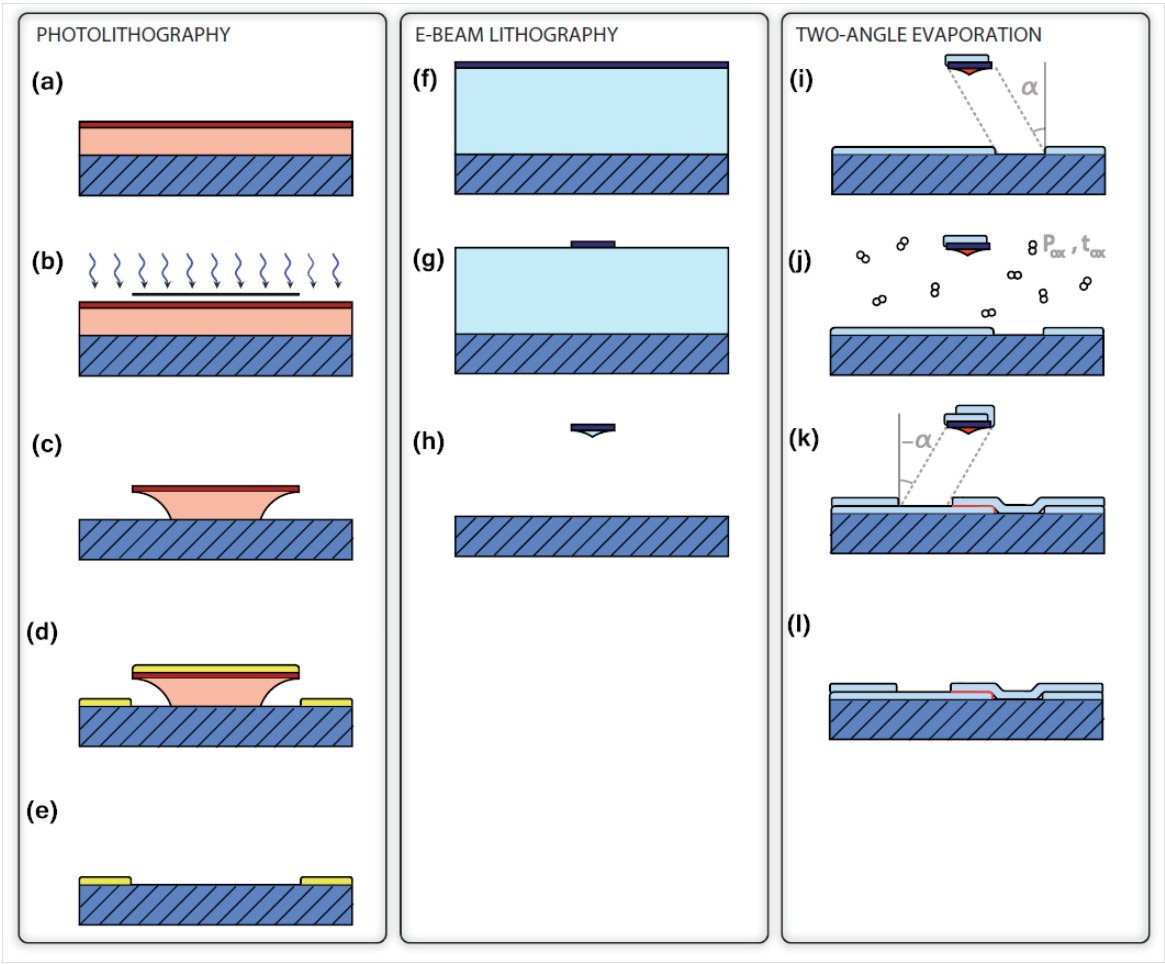

Figure 4.1. The main steps of the fabrication processes. (a)-e describes the photolithography process used to de_ne and deposit the contact metals used for bond pads, ground planes and test structures. In (f)-(h), the electron beam lithography process is used to de_ne the Dolan bridge for the Josephson junctions, as well as the superconducting resontor. Finally, the junctions are evaporated using two-angle evaporation, shown in (i)-l [49].

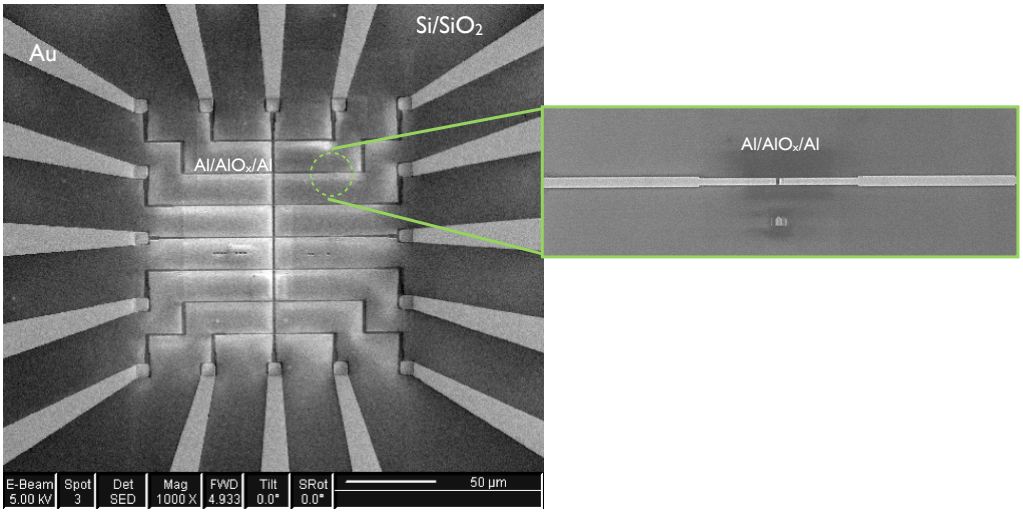

Figure. 4.2. SEM image showing the overview of a chip used in this work. A representative junction is displayed in the magnified box.

Chapter 5

Microscopy and Specimen Preparation

As we aim to understand the quality functional structure of the $Al/AlO_x/Al$ junctions, high performance analytical tools are needed to study the microstructure of these samples. Naturally, specimen preparation is an important issue for having high quality results. In this chapter we will explain the principles of different electron microscopes that have been used in this work. Also, the different specimen preparation techniques used in this study will be introduced.

5.1 Microscopy

5.1.1 Scanning Electron Microscope (SEM)

SEM is one of the most powerful and adaptable instruments for examination and analysis of the solid objects microstructures. This microscope provides information about surface topography, composition and crystal orientation of the specimens. The high spatial resolution, around 1 nm, and also the large depth of field of the SEM make it very suitable for topographic imaging [51].

5.1.1.1 Principles of SEM

In the SEM convergent electron beam scans across the specimen surface and interacts with the electrons in the specimen. This interaction generates different types of signals that can be detected and used both for imaging and chemical analysis (Figure 5.1).

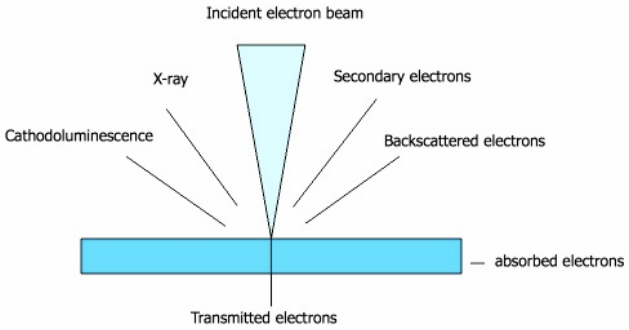

Figure 5.1. Example of different types of signals produced when high-energy electrons interact with a material

Figure 5.2 shows the basic setup of an SEM. The electron column, which consists of the electron gun and the electromagnetic lenses, provides the electron beam in vacuum. The electrons are generated by the electron gun (e.g. W, LaV_6 or a field emission gun (FEG)) and accelerated to an energy of 0.1-30 keV. In order to scan the specimen with a small electron beam, the beam passes through a set of electromagnetic lenses including condenser lens, objective lens and apertures. Before the electron beam reaches the condenser lens, it losses the furthest electrons away from the optical axis by passing through a fixed aperture. The condenser lens demagnetizes the image of the electron source and defines the size of the electron probe on the specimen, the spot size. Afterwards, the electron beam passes through the objective lens with an objective aperture. This lens focuses the probe on the specimen. The scan coils sweep the beam across the specimen in the x- and y-direction. The magnification (*M)* of the image is the ratio between the fixed length displayed on the viewing screen and the corresponding scanned length on the specimen [51-52].

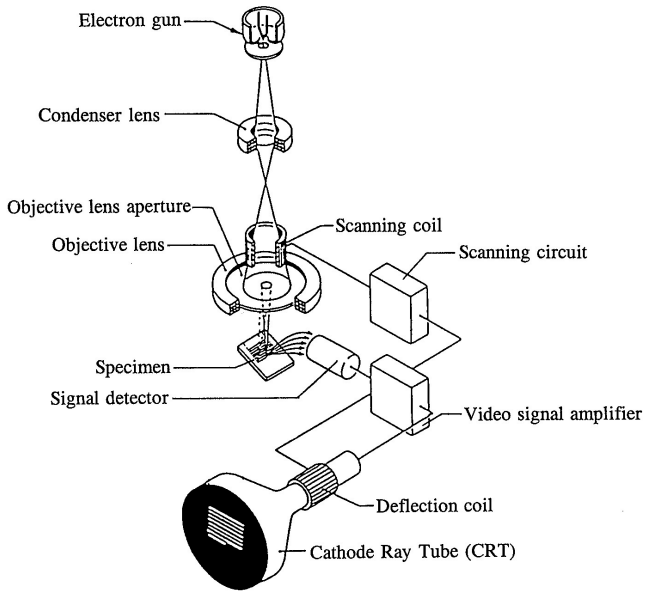

Figure 5.2. Schematic of SEM, showing the main components of the electron column and the data collection [53].

5.1.1.2 Image Formation

Once the electron beam impinges on the specimen, different kinds of signals are generated that can be collected by a set of different detectors and displayed as an image. The detector converts the signals to point-by-point intensity changes on the screen and forms an image. Secondary electrons (SE) and Backscattered electrons (BSE) are the most common signals used for imaging and they are generated from different depths of the specimen. When the electron beam enters the specimen, it scatters and spread out into a teardrop-shaped volume of the material, called the interaction volume, from where the SE and BSE are generated (Figure 5.3).
The interaction volume depends on different parameters such as beam energy, atomic number and specimen surface tilt (Figure 5.4). SEs are electrons formed from regions close to the surface by inelastic scattering of primary incoming electrons, SE I (Figure 5.5). The outgoing BSE can also generate SE signal (SE II) but this signal mostly contributes to the background [51].

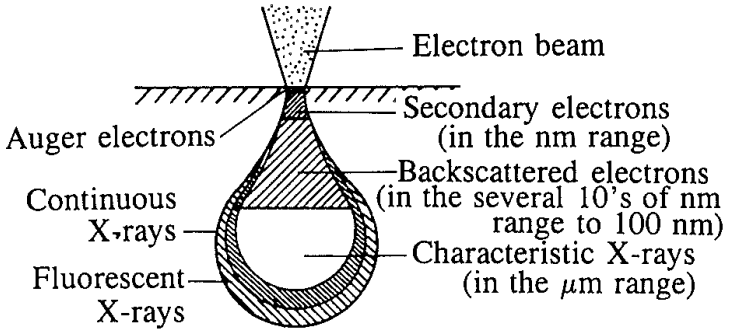

Figure 5.3 The interaction volume indicating where SE, BSE and X-rays are generated [53]

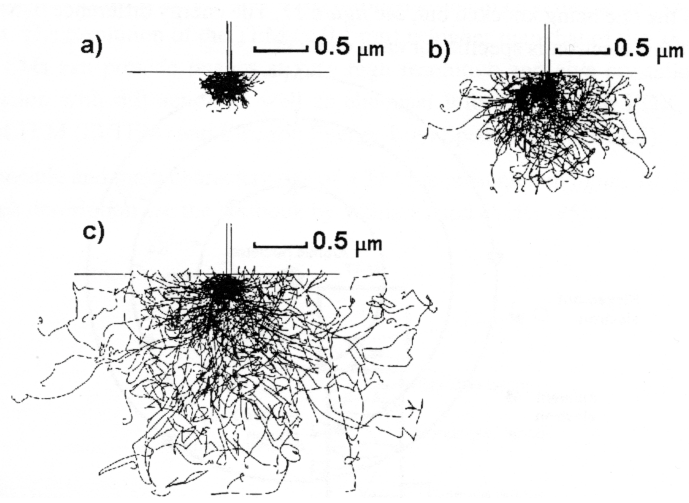

Figure 5.4 Beam energy impact on the interaction volume (Fe) from Monte Carlo simulations. a) 10 keV b) 20 keV c) 30 keV [51]

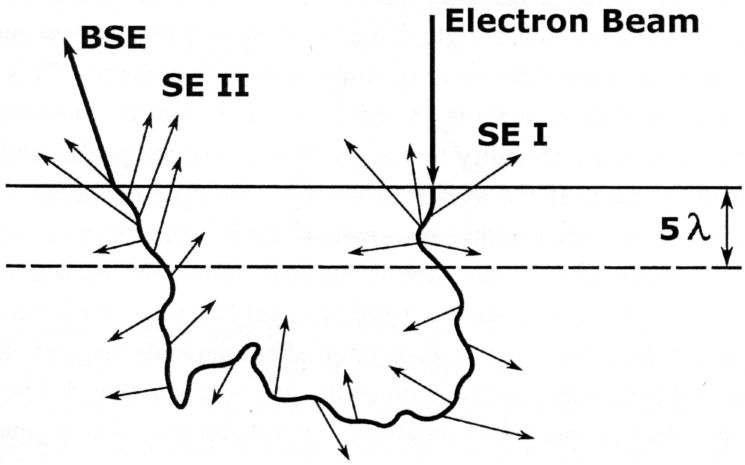

Figure 5.5 Generation of SE I, SE II and BSE. λ is the mean free path for SE [51].

SEs are low energy electrons that provide a high-resolution image with topographic contrast. The topography contrast is indebted to the low energy of SE and the ability of the detector to attract and collect the signals even though the trajectory line does not point directly towards the detector. For instance by applying a small positive voltage to the detector, it can collect signals from edges, corners and cavities, which are spread in all directions, (Figure 5.6). BSEs on the other hand are generated by elastic scattering, with nearly no energy loss, from regions deeper below the surface of the specimen and escape through the surface with straight trajectories. The detector only detects the BSE signals travelling directly towards the detector as it is shown in Figure 5.6. BSE have more energy and come from a larger volume, therefore they give rise to images with less resolution compared to SE. On the other hand, since the amount of BSE depends on the sample's composition it can give good compositional contrast image. An element with higher atomic number (Z) gives more BSE and appears brighter in the image than an element with lower atomic number [51].

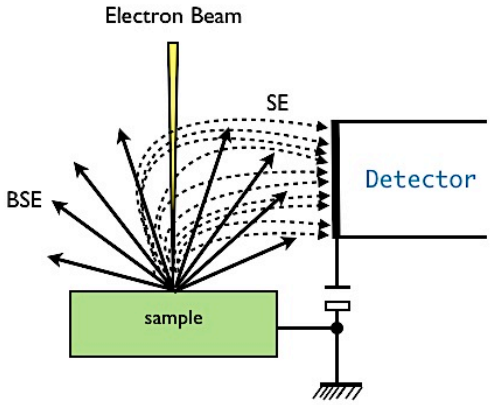

Figure 5.6 Comparison of the signals from SE (low energy) and BSE (high energy)

SEM can also perform chemical analysis, Energy Dispersive X-ray Spectroscopy (EDX/EDS) by using the X-ray photons. The details of EDX analysis are explained in a later TEM section.

Our SEM investigations were carried out with a LEO ULTRA 55 FEG SEM operated in high-vacuum mode. The information obtained from these measurements was mainly morphological data from SE.

5.1.2 Focused Ion Beam (FIB)

The focused ion beam (FIB) workstation is very similar to SEM. It contains a gun, a column with magnetic lenses, a specimen chamber and detectors for image formation. A computer does the processing job of the signals, as well as displaying the image on a screen. The main difference is that this microscope uses Ga^+-ions instead of electrons and the gun is a liquid metal source (LMIS) containing a small reservoir of liquid Ga-metal. The source gets heated by applying a current and generates Ga^+-ions. Thereafter, the ions are accelerated in a potential field, typically 30 kV, through the column (Figure 5.7). By changing the size of the beam acceptance aperture, the beam current can be controlled. A low current beam can be used for imaging the specimen and a high current beam is powerful enough to etch or pattern the specimen. This ability can be used for e.g. micromachining or sample preparation [54].

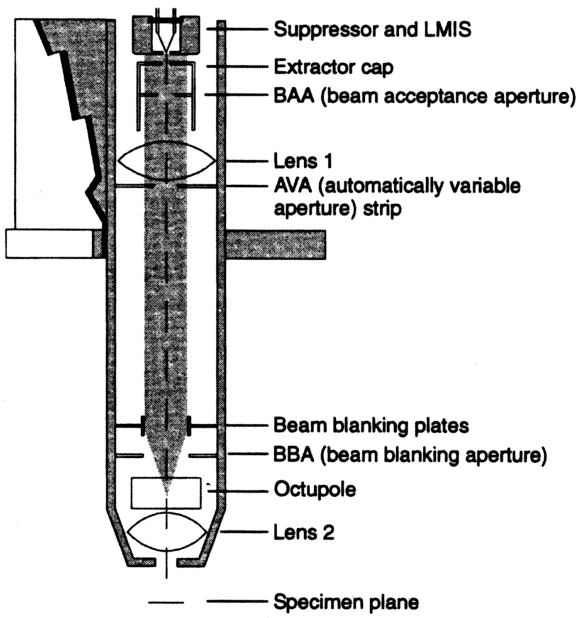

Figure 5.7 Schematic drawing of the ion column [54]

5.1.2.1 Focused Ion Beam / Scanning Electron Microscopy (FIB/SEM)

Combining the two methods of FIB and SEM into one instrument (FIB/SEM), results in a potent tool for manipulating specimens while at the same time having access to good imaging possibilities. In this work a FEI Strata DualBeam 235M has been used. In this setup the electron source is positioned right above the sample, while the ion source is emplaced with a 52° angle with respect to the electron column (Figure 5.8). This microscope is equipped with a gas injection system (GIS), which consists of a reservoir of metal-organic precursor gas (i.e. $(CH_3)_3CH_3C_5H_4Pt$) and a distribution needle for deposition of Pt layers on the specimen surface. Moreover, this instrument has a movable micromanipulator needle, a so called Omniproble, which is a tool used in the lift-out procedure, where thin lamellas are cut out and extracted from a bulk specimen for further analysis in the TEM [54].

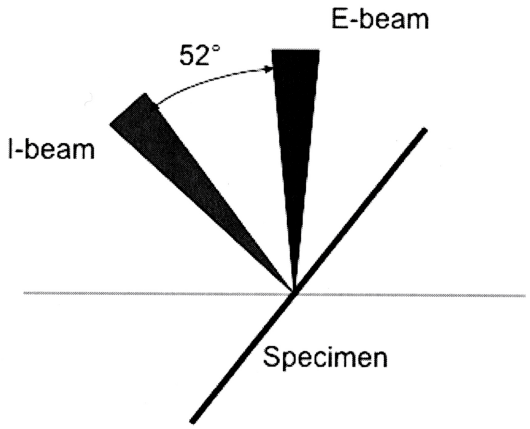

Figure 5.8 Cross-sectional schematic of the electron and ion beam in a FIB/SEM

5.1.3 Transmission Electron Microscope (TEM)

TEM is similar to SEM in a way that they both produce a beam of electrons a projects it onto the specimen. Hence the construction of the electron gun, condenser lenses and the vacuum system of these two instruments has some similarities. The main differences arise from the way that the images are formed and magnified. In contrast to an SEM, where the signals from a bulk specimen are detected from a position above the specimen; in a TEM the electron beam interacts with and is transmitted through the thin electron transparent specimen foil. The transmitted electrons are projected on a fluorescent screen or on a camera beneath the specimen. TEM can provide images with sub-Å resolution as well as crystallographic information. Besides, chemical information can be obtained by EDX, Energy Filtered TEM (EFTEM) and Electron Energy-Loss Spectroscopy (EELS) [55].

The principle set up of a TEM is shown in Figure 5.9. This system is composed of three basic parts: the illumination system, the image forming system and the projection system.

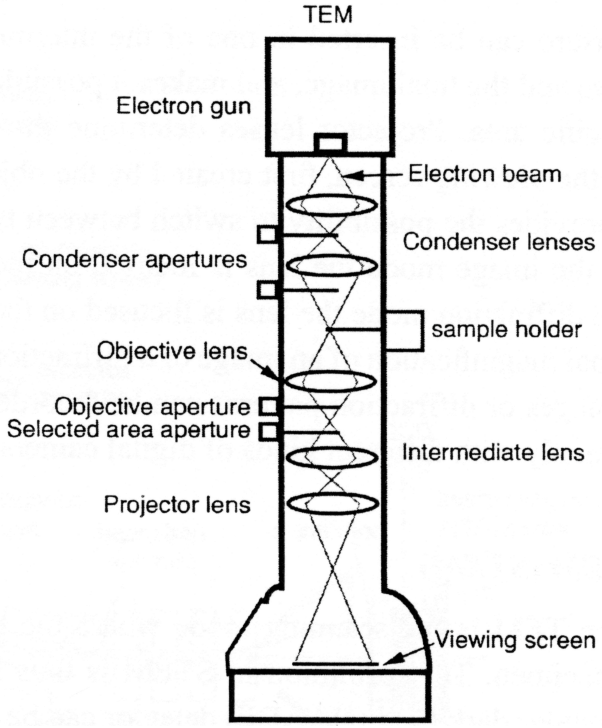

Figure 5.9 Schematic drawing of a TEM [56]

5.1.3.1 Illumination system and specimen stage

The illumination system consists of an electron gun, which generates electrons and forms a first beam crossover, and two or three condenser lenses, which focus and de-magnify the image of the electron source. There are three common types of electron guns, thermionic tungsten hairpin filament, thermionic LaB_6 crystal and Field Emission Gun (FEG) consists of a single crystal of tungsten. The FEG source gives a better energy resolution and coherency as well as a higher brightness compared to the two other sources. The emitted electrons are accelerated through a potential field, typically between 80 to 300 kV, in the column.

The first condenser lens, C1, determines the minimum obtainable electron beam diameter on the specimen, the spot size, by demagnification of the gun crossover.
C2, the second condenser lens, controls the convergence angle of the beam and also focuses the electron beam on the specimen (varying intensity). C1 and C2 are equipped with apertures that can block electrons with large convergence angles. This helps to improve the resolution because the further away the electrons are from the optical axis the more they suffer from lens aberrations. New TEMs can have a third condenser lens that allows the adjustment of the beam convergence independent of the C2 aperture and allows the parallelism of the beam to be adjusted in TEM mode. The specimen is placed in a specimen holder, which allows for tilting the specimen around one or more axes, and thereafter inserted into the TEM stage. As a rule of thumb the specimen should have a thickness of less than 100 nm in order to be electron transparent. The optimum sample for high resolution imaging is as thin as possible and has an even thickness [55].

5.1.3.2 Image Formation System

The objective lens and its aperture constitute the image formation system of a TEM and they determine the spatial resolution of the image. The objective lens forms the first image and the diffraction pattern of the specimen. There are two main operating modes in a TEM, diffraction and imaging, where either the diffraction pattern or the image is projected onto the screen or the camera. As can be seen in Figure 5.10, the ray diagram of these different modes, the diffraction pattern is formed in the back focal plan of the objective lens while the image is formed in the image plane [55].

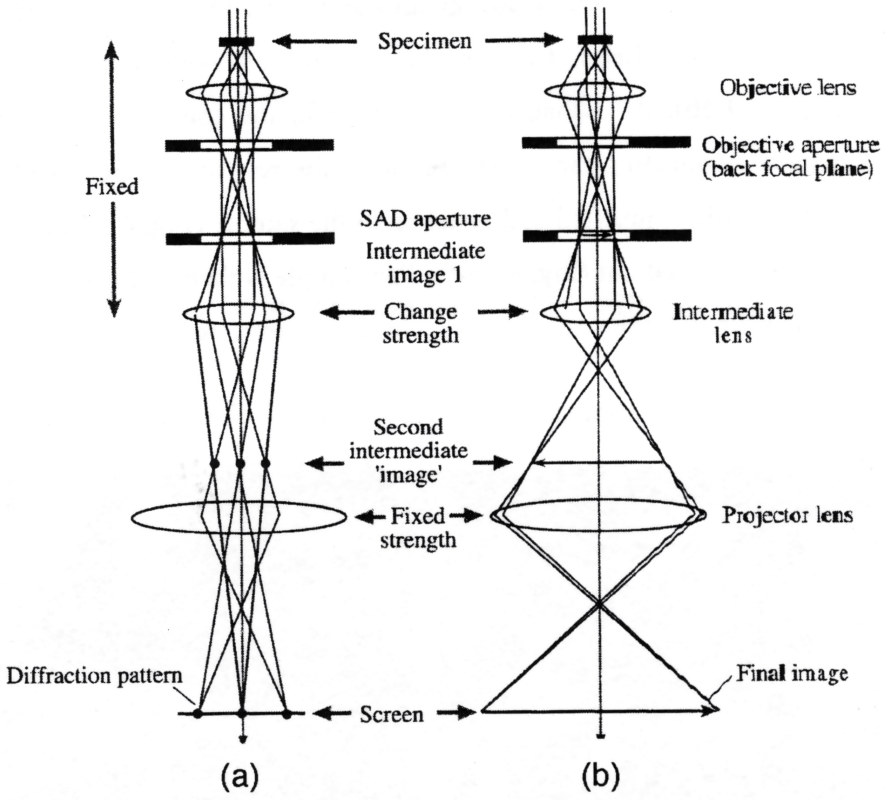

Figure 5.10 Ray diagram for the different modes in TEM: (a) diffraction mode and (b) imaging mode [55]

5.1.3.2.1 Electron Diffraction

In diffraction mode crystallographic information of the specimen can be acquired. Diffraction occurs when electrons of the primary beam are scattered elastically in the specimen. Electrons, which are scattered by the same planes of atoms in the specimen, will leave the specimen in parallel directions and therefore meet in the same "spot" in the back focal plane of the objective lens. If the material is crystalline the diffraction pattern from small regions of the specimen will consist of distinct diffraction spots where the distance and angle between the spots provide information

about the distances and angles between the atomic planes in the specimen. A polycrystalline specimen with randomly oriented grains produces a circular pattern. On the other hand, an amorphous material will give a diffuse ring pattern due to the lack of long range ordering.

Diffraction pattern from a specific area can be studied individually by inserting a selected area aperture in one of the intermediate image planes, between the specimen and the final image. Using this method, *selected area diffraction* (SAD), the orientation of individual grains or film layers can be determined [55].

5.1.3.2.2 TEM Imaging

The objective lens forms an image in the image plane and the objective lens aperture, which sits in the back focal plane of this lens; selects the electrons that will contribute to the image, and thereby affect the appearance of the image. If the aperture is inserted in a way that only the central (non-scattered) beam is selected, a bright field (BF) image will be obtained. By choosing a diffracted beam a dark field (DF) is obtained. This can be done either by shifting the objective aperture off-axis to the diffracted spot or by tilting the diffracted beam into the optic axis (centered DF) (Figure 5. 11).

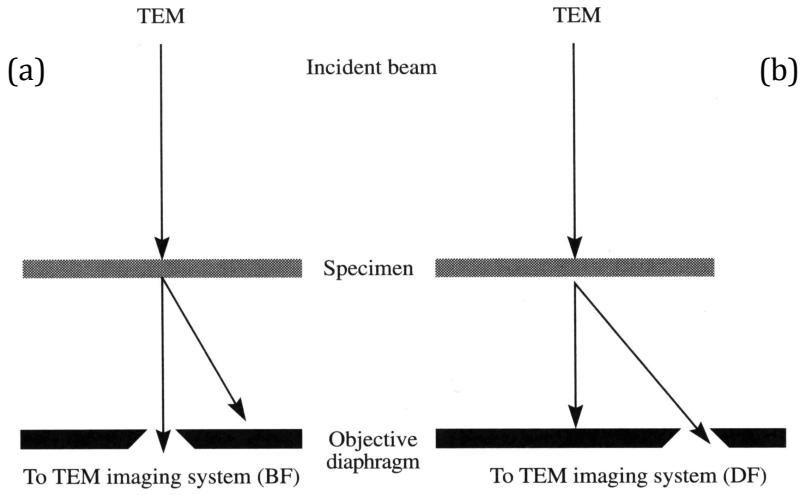

Figure 5. 11 Position of objective lens aperture for forming (a) bright field image and (b) dark filed image [55].

The objective lens aperture can also improve the contrast of the final image. By selecting one beam, only amplitude contrast contributes to the image formation. There are two types of amplitude contrast, mass-thickness contrast and diffraction contrast. For mass-thickness contrast the scattering power of different areas of the specimen is visualized. This type of contrast is strongly depended on the atomic number (Z) and thickness of the material. The areas with higher atomic number and greater thickness scatter electrons more strongly and therefore appear dark in the BF images and bright

in DF images. Diffraction contrast arises from coherent elastic scattering of electrons through specific angles governed by Bragg's law. In a BF image, areas that appear dark correspond to areas where the Bragg condition (Figure 5.12), is fulfilled for certain atomic planes, resulting in strong diffracted beam and consequently a reduced intensity of the direct beam [55].

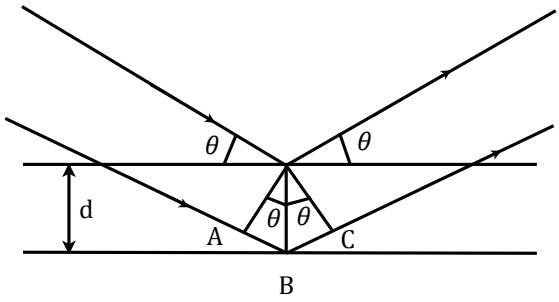

Figure 5. 12 The Bragg law, $n\lambda = 2d \sin\theta_B$, describes diffraction in terms of the reflection of plane wave (wavelength λ) incident at an angle θ to atomic planes of spacing d [55]

5.1.3.2.2.1 Lens Aberrations

The magnetic lenses used in electron microscopes have some imperfections that limit the resolution of the microscope. There are ten kinds of lens defects but here we will mention only three of them that limit the microscope performance significantly.

Spherical aberration (Cs): this aberration arises from the inhomogeneity of the lens field, which affects the off-axis rays. The further off-axis an electron is, the more strongly is it bent back towards the optical axis (Figure 5.13) and as a result a point object is imaged as a disk. This effect limits the ability to resolve fine scale details because the imaging process blurs the features. Eventually, the resolution of TEM is limited by this defect.

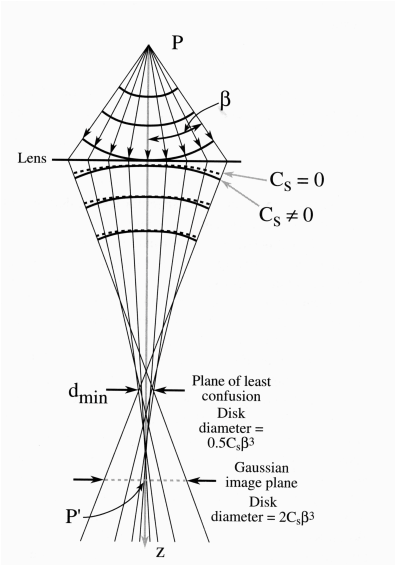

Figure 5. 13 Spherical aberration in the lens causes wave fronts from a point P to be spherically disordered and being imaged as a disk [55]

Chromatic aberration (Cc): as the name emphasizes this aberration is related to *color* or in fact the wavelength and thus energy of the electrons. The electrons of the beam are assumed to be monochromatic but as the beam passes through the specimen, electrons of a whole range of energies spring from the thin foil. When these electrons reach the objective lens, those with lower energy will be bent more strongly and therefore electrons from a point in the object form a disc in the image plane (Figure 5.14).

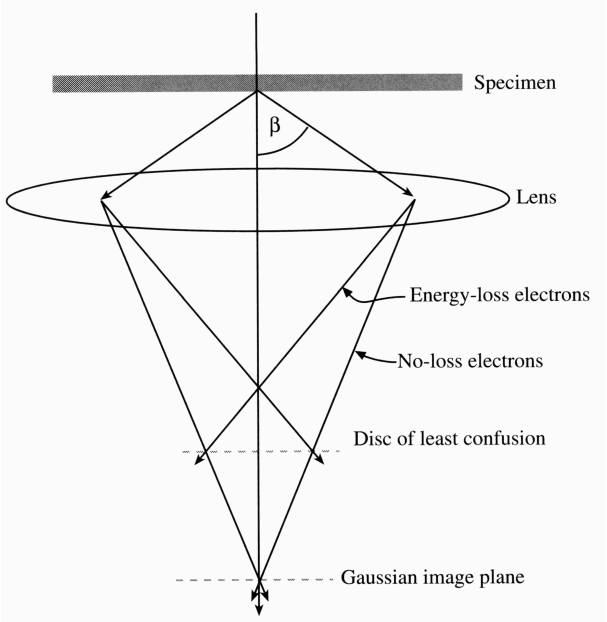

Figure 5.14 Chromatic aberration results in electrons with a range of energies being focused in different planes [55]

Astigmatism: having a non-uniform magnetic field while the electrons curl round the optic axis, results in astigmatism. This aberration emerges from the limitation of making perfectly cylindrical soft iron pole pieces for the magnetic lenses and also local variations in the magnetic field due to microstructural inhomogeneity of the soft iron. Moreover, inserting an aperture can disturb the magnetic field of the lens and if there is contamination on the aperture it may get charged and deflect the beam. Using small octupoles, which provides a field to balance the unwanted field inhomogeneities, can correct for the astigmatism. These octupoles are called stigmators [55].

5.1.3.2.2.2 High-resolution TEM

A third type of image formation is High Resolution TEM (HRTEM), which is based on phase contrast. Here the objective aperture selects *several* diffraction spots in the back focal plane and forms the image in the image plane at high magnification (Figure 5.15).

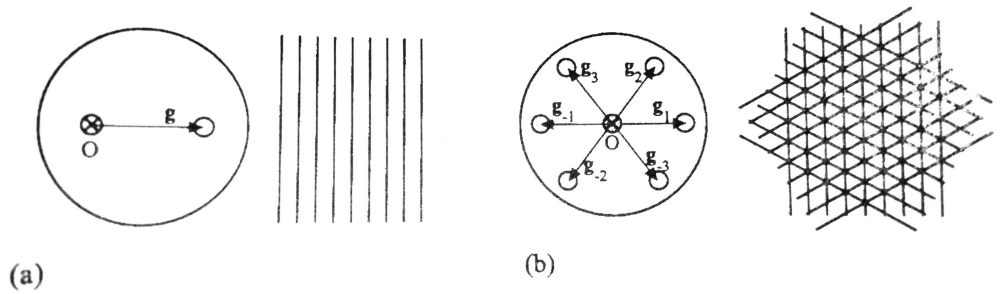

Figure 5.15 (a) Schematic two-beam image showing fringes perpendicular to the diffracted beam. (b) many-beam image showing crossing lattice fringes and its corresponding diffraction pattern [55]

In order to understand the resolution limits in a HRTEM image, one can consider the objective contrast transfer function (OCTF) shown in Figure 5.16.

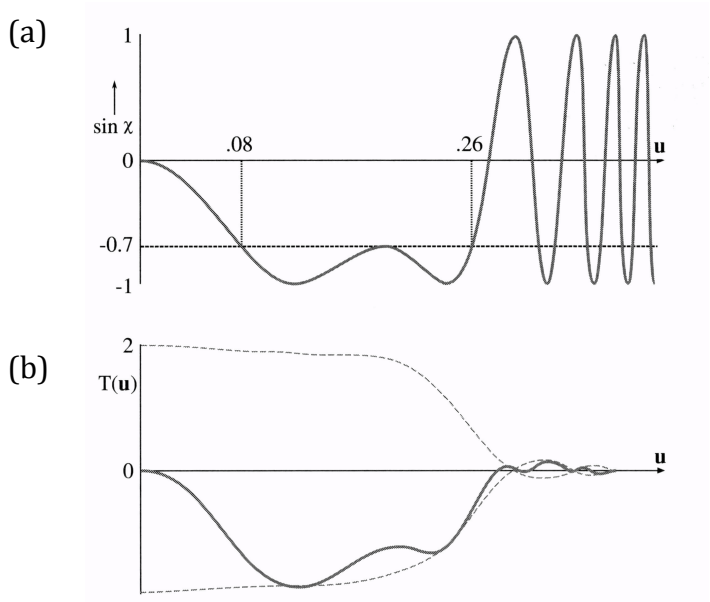

Figure 5. 16 (a) sin *X(u)* versus *u* without damping of the higher spatial frequencies, (b) the objective transfer function, *T(u),* modified by the damping envelope function, *E(u)* (dashed line) [55]

$$OCTF = T(u) = A(u)E(u)\underbrace{2\sin\chi(u)}_{B(u)} \quad (5.1)$$

Where

$$\chi(u) = \pi\Delta f\lambda u^2 + \frac{1}{2}\pi C_s\lambda^3 u^4 \quad (5.2)$$

$A(u)$ is the aperture function, $E(u)$ is the envelope function, $\chi(u)$ is the phase-distortion function, Δf is the defocus, λ is wavelength of the electrons and u is the reciprocal distance. Without the envelope function the OCTF can oscillate between -1 and +1, though higher orders of aberrations like chromatic aberration (C_c) and instabilities may damp the OCTF amplitude. The information limit arises from the point where the contrast is damped and goes towards zero, which should not be mixed with the local zeros during the oscillation. When the OCTF is negative, the *atoms* in a HRTEM image appear white on a black background and when it is positive it gives a reverse contrast. The first zero that appears in the oscillation gives the smallest distance that can be resolved without contrast inversion and determines the point resolution. The state that the first zero is stretched to its maximum is called Scherzer condition and the corresponding objective lens defocus is then given by

$$\Delta f_{Sch} = -1.2(C_s\lambda)^{\frac{1}{2}} \quad (5.3)$$

From equation 5.3 it also follows that reducing Cs will improve the point resolution. Specimen thickness is another aspect to be considered, because if the specimen is not thin enough additional contrast effects will appear in the image and affect the resolution [55].

5.1.3.3 Projection System

The projection system of a TEM consists of three lenses; one intermediate lens and two projector lenses. The function of the intermediate lens is to magnify the initial image that is formed by the objective lens as well as switching between the two operating modes; imaging and diffraction. For the image mode the lens is focused on the image plane of the objective lens while for the diffraction mode it is focused on the back focal plane of the objective lens. The two projector lenses are setting the final magnification of an image or a diffraction pattern. Recording of the images and diffraction patterns can be done with photographic plates or more commonly digital cameras [55].

5.1.3.4 Scanning Transmission Electron Microscopy

In this mode the microscope lenses are adjusted to create a focused convergent electron beam at the sample surface. This focused beam is then scanned across the sample and transmitted electrons are collected point-by-point to form an image. The resolution in STEM is therefore limited by the probe size and the limit is given by

$$d_{min} = 0.43 {C_s}^{1/4} \lambda^{3/4} \qquad (5.4)$$

where d_m is the minimum beam diameter, C_s is the spherical aberration and λ is the wavelength of the electrons. The shape of the beam depends on the convergence angle and defocus. With increased convergence angle a sharper beam is obtained due to less aperture diffraction.

In STEM mode electrons with different scattering angles can be selected and detected. Collecting electrons with low scattering angle (<10 mrad), including the non-scattered electrons, provides a BF image. A DF image can be obtained by using an annular dark field (ADF) detector to collect electrons scattered at higher angles while the zero loss beam is omitted. For angles between 10 and 50 mrad the contrast is obtained from Bragg diffraction. For electrons scattered with angles above 50 mrad, a high angular annular dark filed (HAADF) detector is used and the contrast arises from atomic number (Z). The heavier the atom is, the higher the intensity in the image [57].

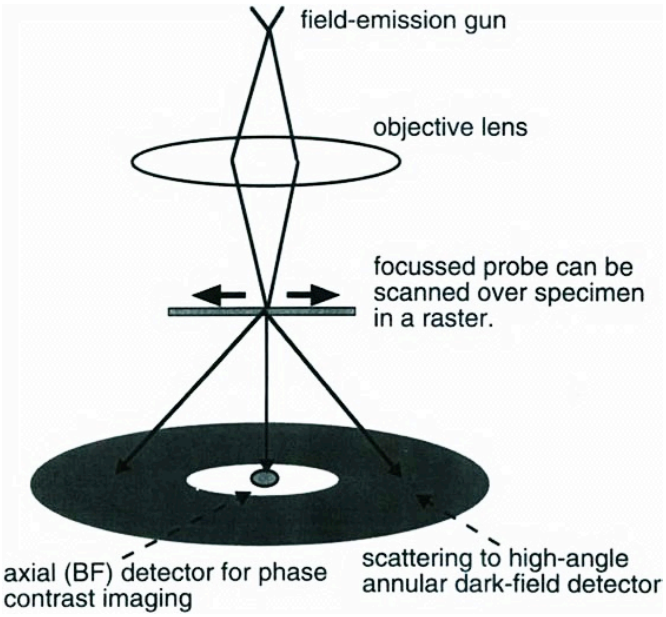

Figure 5. 17 Schematic of the scanning transmission electron microscope (STEM) showing the configuration of the annular dark-field (ADF) detector, and the bright field (BF) detector [57].

5.1.3.4.1 Spherical Aberration (C_s) Corrected STEM

The development of spherical aberration (C_s) correctors in the recent years, made further improvement of the spatial resolution of STEM achievable. As it is shown in equation 4.2, the beam diameter is determined by the Gaussian diameter of the gun, broadening effects from C_s and diffraction from the final aperture.

$$d_t = \left(\left(\frac{2}{\pi} \left(\frac{i}{\beta} \right)^2 \frac{1}{\alpha} \right)^2 + \left(0.5 C_s \alpha^3 \right)^2 + \left(1.22 \frac{\lambda}{\alpha} \right)^2 \right)^{1/2} \qquad (5.5)$$

Where i represents beam current, β brightness, α the convergence semi-angle and λ the wavelength of the electrons. Increasing α causes increment of the middle term and decrement of the two other terms. Therefore, if C_s gets smaller or become zero the beam diameter can be reduced and consequently the resolution will be improved. The present state-of-the-art microscopes with probe C_s correctors can achieve a resolution down to 0.7 Å. Nevertheless, correctors for even higher order of aberrations such as chromatic aberration (C_c) have been developed and prompted further improvement in resolution. However, C_c corrected microscopes only exists in three institutions and are still being investigated [58-59].

5.1.3.5 Analytical TEM

5.1.3.5.1 Energy Dispersive X-ray Spectroscopy (EDX/EDS)

The signals generated from the interaction between the electron beam and the specimen X-ray photons, can be used for chemical analysis. These photons carry information about the elements present in the specimen, and enable qualitative (elemental identification) as well as quantitative analysis (elemental concentration).
As an electron with high enough energy, knocks out a core electron from an atom thereby ionising the atom, X-rays can be emitted by relaxation of the atom. The relaxation occurs when an electron from an outer shell takes the place of the one being knocked out, Figure 5.18. The energy difference between these two electron states is specific for each element and facilitates elemental identification.

Analysing and quantifying EDX data, one should consider many parameters, for instance the atomic number. Light elements release low energy photons, which are difficult to quantify with high accuracy due to absorption effects, especially in matrices containing heavy elements, but also in the detector itself. Another issue is the energy resolution of the detector that can limit the possibility to resolve closely spaced spectral lines, as well as overlapping lines, which is a major problem if the specimen contains several elements. EDX data for quantification is corrected with a so-called "ZAF" correction in order to compensate for these three effects: the atomic number effect, the absorption effect and the fluoresce effect. The atomic number effect is related to the efficiency with which an element can produce X-ray photons. The absorption effect is related to the mass absorption of elements and how much the

intensity is diminished. The fluorescence effect is a challenge in a specimen with several elements where higher energy X-rays passing through the specimen can excite lower energy radiation. The spatial resolution of this analysis is much better in the TEM due to the thin specimens which limit beam broadening, thereby significantly reducing the interaction volume compared to bulk SEM samples [51-52], [55].

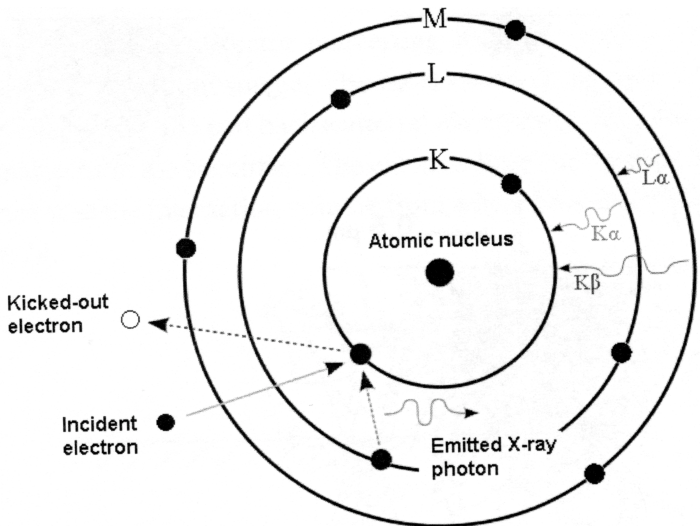

Figure 5. 18 The principle of EDX. An incident electron knocks out a core electron and an outer shell electron takes its place [60]

5.1.3.5.2 Electron Energy Loss Spectroscopy (EELS)

Electron energy loss spectroscopy (EELS) is an analytical technique that inquires into the electronic structure of atoms in a material. This is fulfilled by measuring the energy loss of the transmitted electrons that scattered inelastically when interacting with the specimen. In order to do such measurements the TEM should be equipped with an energy filter system, which can be mounted after the microscope column, Gatan Image Filter (GIF), or in-column, Omega filter. The TEMs used in this study have a GIF system, which will be described briefly. The set up of a GIF is shown in Figure 5.19. The beam of transmitted electrons is directed into the GIF, the entrance to this system is usually bellow the fluorescent screen and/or a camera. The transmitted electrons are then deflected in a magnetic sector to an angle close to 90°. Afterwards, they pass through an energy selective slit followed by a projector system with a set of quadrupoles and sextupoles, which corrects for aberrations and astigmatism. At the rear end a CCD camera is positioned for collecting the data. It can either be in image mode, for a filtered image, or in spectroscopy mode for EELS [55].

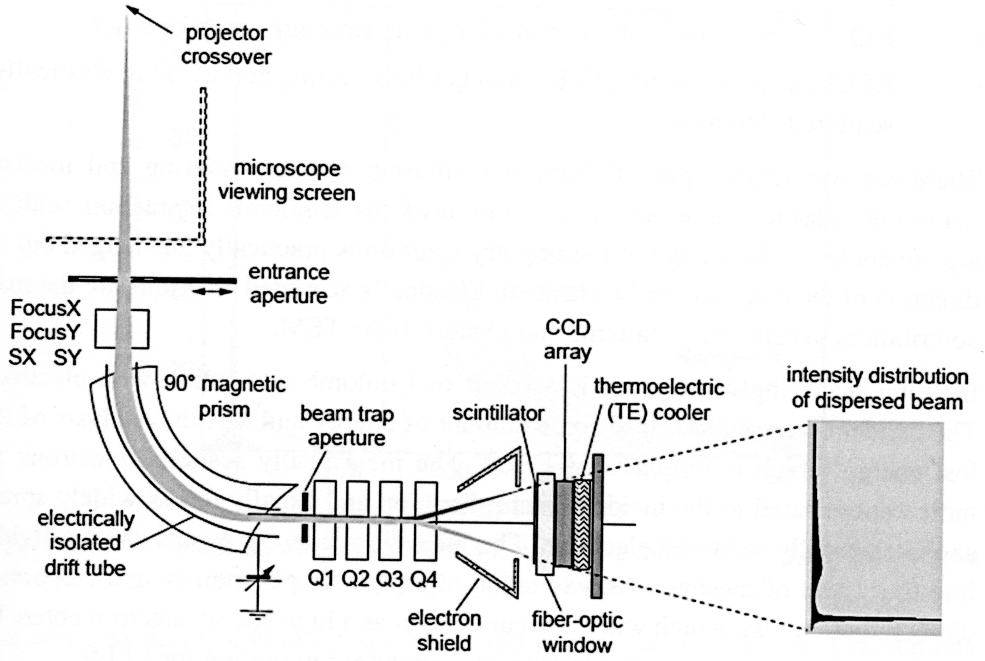

Figure 5. 19 A schematic drawing of a GIF [61]

The collected data from the GIF in spectroscopy mode, which appears as an EELS spectrum (Figure 5. 20), can provide information about the identity of elements in the specimen as well as their concentration. Besides, it unveils the electronic structure and properties of the specimen.

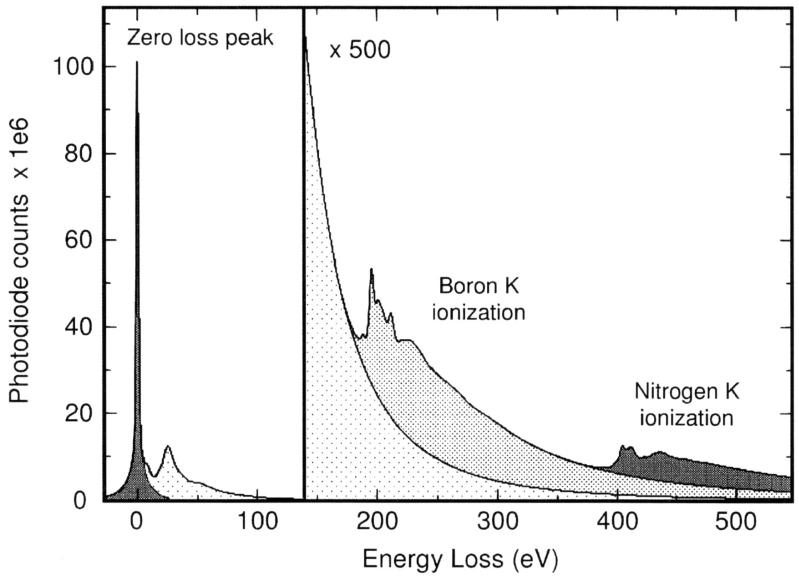

Figure 5. 20 A schematic drawing of an EELS spectrum with the zero-loss peak and core-loss regions. This is an example with boron and nitrogen [61]

As is shown in Figure 5. 20 the spectrum displays the intensity of the scattered electrons as a function of their energy-loss and can be divided in three regions, zero-loss region, low-loss region and high-loss region.

I. In the zero-loss region elastically scattered electron and also electrons that hardly lost any energy while passing the specimen, appear as a zero-loss peak. This peak is narrow and indicates the energy resolution of the spectrum.

II. Electrons that lost energy less than 50 eV can be seen in the low-loss region. This region provides information about the interaction with weakly bounded outer-shell electrons.

III. The high-loss region contains losses above 50 eV and the interactions between the transmitted and core electrons are monitored. These inelastically scattered electrons give rise to characteristic ionization edges in the spectra. These edges have a specific on set energy and shape for each element and therefore the elements present in the specimen can be identified. Moreover, quantitative information about an identified element can be obtained because the intensity beneath each edge is proportional to the number of atoms of an element present in the examined area of the specimen. The fine structure of an edge indicates the unoccupied electron density of states above the Fermi energy and contains information about the crystallographic structure and energy-band structure of the specimen [62-63].

5.1.3.5.3 Energy Filtered TEM (EFTEM)

By inserting a slit with variable width in the GIF it is possible to choose an energy interval in the spectrum, allowing only electrons that have lost that particular amount of energy to pass through to the CCD camera and form an energy-filtered image. If the chosen energy window corresponds to an ionization edge, “elemental mapping” of a specific element can be obtained. There are two ways of creating such a map, the three-window technique or the two-window technique, also called the jump ratio method. In the three-window method, two windows prior to the edge (pre-edge window 1 and 2) and one window after the edge (post-edge window) are chosen by positioning the energy selecting slit at these specific energies (Figure 5. 21). An extrapolation of the background is calculated from the two pre-edges and then subtracted from the post-edge window, which results in a quantitative elemental map. Jump ratio images are calculated by dividing the post-edge and the second pre-edge window (the one closest to the ionization edge). This method is mainly used for qualitative filtered imaging, as it is less sensitive to thickness effects and diffraction conditions [55].

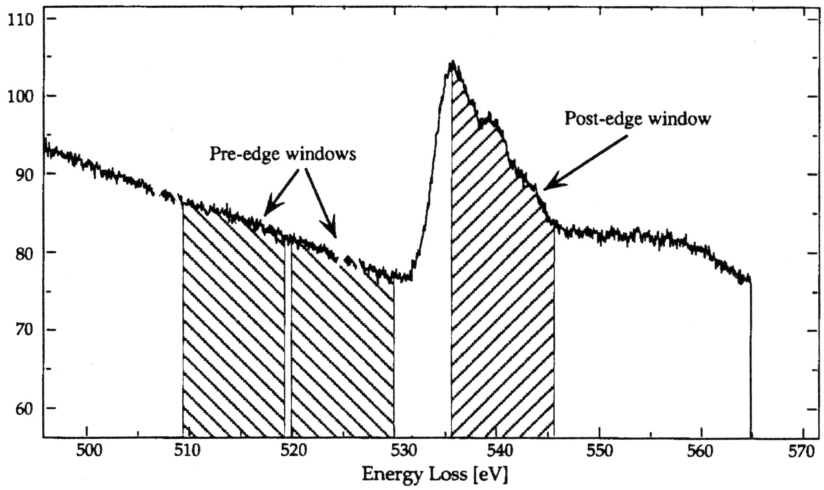

Figure 5. 21The energy-windows used for elemental mapping [55]

5.2. Specimen preparation

Obtaining high quality data, both imaging and spectroscopy, from TEM requires specimens with superior quality. In order to prepare our TEM specimens we have used two different techniques: the lift-out technique in the FIB-SEM, which was used for extraction of a single junction from the patterned samples and conventional technique for the non-patterned samples.

5.2.1 Lift-Out Technique

Extraction of nanoscale devices such as the Al/AlO_x/Al junctions requires special preparation techniques. One of the handiest instruments for making site-specific TEM specimens with potential high quality is the FIB/SEM [64-68]. As was explained in the microscopy section, the FIB is used for machining the sample and the SEM is used for checking and imaging the sample without causing any destructive effects. However, extraction of such small structures is not straightforward. The exact position of the area of interest can easily be lost by specimen charging or beam drift. Moreover, for a low contrast material such as Al it is difficult to find a reference mark that can be used as an indication of when to stop milling and for drift compensation. Therefore, we developed a method to increase the accuracy and success rate for preparing high quality TEM specimen of nanoscale and local microstructural features [69]. The steps of this method are as following; 1) identifying of the area of interest (AOI) with SEM (i.e. the desired junction), 2) deposition of a protective cap of Pt over the AOI (by electrons), 3) milling location marks on either side of the AOI, 4) deposition of a second protective layer of Pt (by ions), 5) cutting the AOI, lifting out and attaching it on a TEM grid, 6) thinning of the specimen using the location marks as end detection points. The detailed parameters used for extraction of a tunnel junction are explained in paper I.

5.2.2 Conventional Technique

This technique is based on grinding, polishing and ion milling. We used this method to make both cross-sectional and plan-view TEM specimens from the non-patterned samples. As the name emphasizes the first method provides a cross-sectional view of the junction as well as the film/substrate interface. On the other hand, a plan-view specimen can give sensible information about the grain size distribution of the Al layers. The general procedure of cross-sectional TEM sample preparation is illustrated in Figure 5. 22 [56, 70]. For grinding and polishing of the samples, a tripod was used that gives a high accuracy in controlling the sample thickness. Conjointly with diamond lapping films, which provide a fast procedure and satisfying surface roughness. A Fischione 1010 Ar ion mill was used for thinning down the samples to electron transparency. This ion mill machine is fully programmable and has two independently adjustable Hollow Anode Discharge (HAD) ion sources, which can be operated over a range of extractor voltages (0.5 kV to 6.0 kV) and currents (3 mA to 8 mA). More features of this instrument are the milling angle in the range of 0 to 45 °, specimen rotation or rocking and an optional liquid nitrogen cooled specimen stage [71].

The ion-milling step is the most sensitive step in conventional sample preparation and specimen quality is strongly dependent on the choice of milling energy and angle. This procedure is also material dependent and the milling parameters should be optimized for each type of material. For our specimens, milling started with higher energy and angle (6kV, 5 mA and 14°), which were gradually reduced to lower values and the final thinning, was done by delicate values (0.7. kV, 5 mA and 8°). Also, in order to reduced the risk of heating the specimen during the milling procedure, the specimen stage was cooled down to almost -100°C by liquid nitrogen.

The procedure of making a plan-view specimen is quite similar to the one for cross-section. But here only one small piece of the cut chip is used and polished from the substrate side while the film is protected.

High resolution analytical TEM was carried out at 300 kV using a probe Cs corrected FEI Titan 80-300 field emission gun TEM with a monochromator, a high energy resolution Gatan Tridiem for spectroscopy and energy filtered imaging, an Oxford energy dispersive x-ray (EDX) detector and a high angle annular dark field (HAADF) scanning TEM (STEM) detector. A Philips CM200 field emission gun TEM operated at 200 kV with an Oxford EDX detector and a Gatan imaging filter and also a Tecnai G2 TEM with a LaB6 gun and EDAX EDX detector and a HAADF STEM detector operated at 200 kV were also used for the structural characterisation.

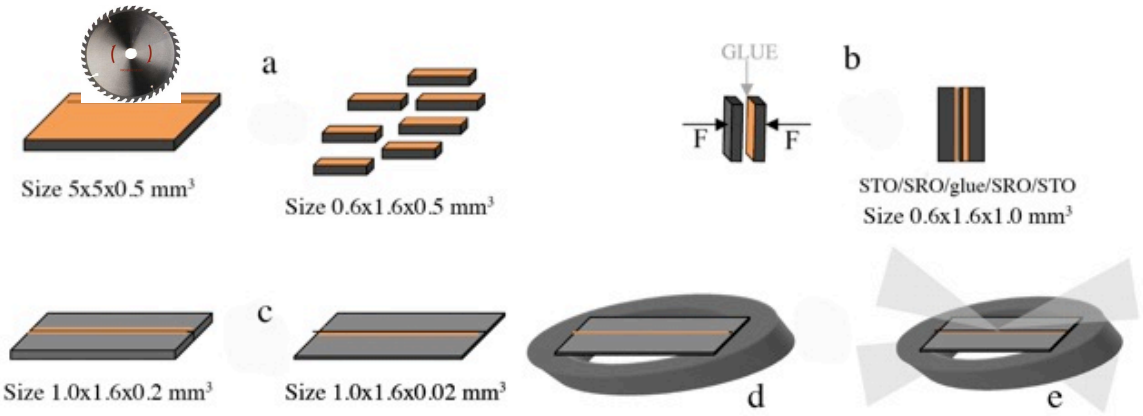

Figure 5. 22 The 7×7mm chips are first cut into smaller pieces with low speed saw (a). Then, using the epoxy M-Bond 610, two equal size smaller pieces are glued together with the film surface facing each other (b). In the next step, the sample is grinded and polished down to a thickness of 20-30μm using a so-called tripod and diamond lapping film (c). This thin sample is then glued to a titanium grid also using M-Bond 610 (d). At the final stage, the sample is ion-milled to reach the electron transparency thickness [56].

Chapter 6

Summery of Appended Papers

This chapter provides brief summery of the appended papers.

6.1 Paper I

A method that enables high precision extraction of transmission electron microscope (TEM) specimens in low contrast materials has been developed. The main idea behind this work is to produce high contrast markers on both sides of and close to the area of interest. The markers are filled during the depositing of the protective layer. The marker material can be of either Pt or C depending on which one gives the highest contrast. It is thereby possible to distinguish the location of the area of interest during focused ion beam (FIB) milling and ensure that the TEM sample is extracted precisely at the desired position. This method is generally applicable and enables FIB/scanning electron microscope users to make high quality TEM specimens from small features and low contrast materials without a need for special holders. We explain the details of this method and illustrate its potential by examples from three different types of materials.

6.2 Paper II

An interaction layer is found at the Al/SiO2 interface in $Al/AlO_x/Al$ tunnel junctions grown on SiO_2 substrates. The amorphous intermixing layer has an average thickness of about 5 nm. We present the detailed structure of this interfacial layer as determined by transmission electron microscopy. The layer contains alumina with aluminum being octahedrally coordinated according to electron energy loss spectroscopy analysis rather than tetrahedrally coordinated, where the latter coordination is the most common type in amorphous alumina. Depth profiles of the Al-O and Si-O bonding characteristics were also investigated using energy loss near edge structure.

6.3 Paper III

The thickness of the tunnel barrier in $Al/AlO_x/Al$ tunnel junctions alters along the junction and might significantly increase at the grain boundaries in presence of thermal grooves. We present a microstructural study of the Al thin films in such a junction. The accurate grain size and source of the surface morphology of the grain have been defined. The normal and abnormal growth mechanisms were observed in these thin films, as well as a strong dependence between the film thickness and the average grain size of the films. Effect of substrate material and temperature on the grain size of the deposited films was studied.

6.4 Paper IV

Most often the microscopic structure of $Al/AlO_x/Al$ tunnel barriers is not considered to be important for the properties of the device and the barrier is often treated as an ideal atomically flat layer with a homogeneous thickness. However, it is now clear that decoherence and noise in quantum devices depend on the microstructure of the tunnel barrier and also the interfaces between the films and the substrate. In this work, the microstructure of $Al/AlO_x/Al$ tunnel barriers was studied using high-resolution analytical transmission electron microscope (TEM). The results show that the polycrystalline Al layers contain columnar grains and the AlO_x barrier is an amorphous layer that follows the topography of the bottom Al layer. The barrier thickness and shape were not dramatically affected by changes in oxidation parameters and the mean thickness of the barrier is 1.3 nm. However, local thickness variations in connection to the grain boundary grooves are observed in each individual barrier.

6.5 Paper V

We show that less than 10% of the barrier area dominates the electron tunneling in state-of-art $Al/AlO_x/Al$ Josephson junctions. They have been studied by transmission electron microscopy, via atomic resolution annular dark field (ADF) scanning transmission electron microscopy (STEM) imaging. The direct observation of the local barrier thickness shows a barrier thickness variation along the junction, from ~1 nm to ~2 nm in the three junctions we studied. The thickness distributions can all be fitted to Gaussian distribution. Moreover, the thickness distribution changes with partial oxygen pressure (p_o) and oxidation time (t_o) while po and to have little impact on the average barrier thickness. The tunnel probability distribution has also been calculated for barriers made at different conditions. It shows that more than 90% of the tunnel current comes from less than 10% of the barrier area in every junction.

Acknowledgments

I would like to express my appreciation to all people who have contributed to this work and helped me.

My sincere thanks go to my supervisor Prof. Eva Olsson for giving me the chance to work with this interesting project and all insightful discussions through my work. I am really grateful to my co-supervisor Prof. Per Delsing for helping me to understand the world of superconductivity through delightful discussions. I express my gratitude to my second co-supervisor Ass. Prof. Stefan Gustanfsson for all the help, input and useful comments to my work.

I deeply appreciate Dr. Tine Greibe for fabricating amazing samples during the first two years of my work. I really enjoyed collaborating with you and learned a lot from you. Now, I should thank the guy who supplied endless number of samples for the last three years, Phili Krantz. My really big thanks go to you for the great collaboration, long long discussions, your positive attitude, kindness and support. Another great appreciation goes to Arsalan for the great discussions, all the help and friendship. I really appreciate Arslan and Michael for being so nice to me through my very frequent visits to their office, tolerating my load and long discussions with Philip!

A sincere thanks goes to Dr. Anders Kvist for the technical microscopy support. Thanks a lot for being so thoughtful, kind and supportive and always answering my weird questions. I learned a lot from you, specially a lot of *Göteborg Jokes*! Another thank goes to Ola for the technical support, nice talks and saving me from computer crises! A special thanks to Robbie Williams! Listening to his songs saved us form falling asleep while we were polishing our specimens!

Nikolina! My Honey! What would I do without you? You are the highlight of my PhD, one of my best friends ever! Big thanks for all day and every day fun, support, kindness and long long talks about everything in life. You always cheer me up. Dostet daram ☺

Henrik! A caring friend full of charm and fun! I deeply thank you for all the things that I learned from you and your constant support and help. I am so lucky to have such a great friend. Kheili mehrabooni ☺

Stefan! The man of seal and potato! You are a talented, creative and funny friend that I can always rely I. Thanks a lot for all the support and fun and listening to my long stories. Kheili bahali ☺

Luciana! I am so happy to get to know you, my sweet and kind friend. Thanks for the charm and happiness that you brought to us whenever you came to Göteborg.

Lunjie! (Dr. Zeng!) I am greatly indebted to you for all the help, kindness, support and great microscopy sessions. You amazingly put up with my constant visits to your office and the daily chitchat of Nikolina and me (the Honeys!).

Olof! A special thank goes to you for sharing the office with me and being kind and understanding. I am impressed that you survived me! ☺

Torben! Many thanks for the help with my thesis cover. It's a piece of art! ☺

Anna! You are such a sweet girl and I always enjoy talking to you. Thanks for your constant support.

Anke, Charlotte, Jenny, Pia, Haiping, Pavleta and Gustav thanks for being so considered and thanks for all the fun during the coffee breaks, lunch and travels. Many thanks to all my former and present microscopy collogues and to Brigita, Josephine, Linda and Lovisa for helping me with administrative details.

I am also grateful to my former collogues in Nanofactory for the nice collaboration.

My friends, Kamellia, Hoda, Andreas, Salma, Alireza, Hengameh, Arsalan, Leili and Ali thanks a lot for always cheering me up and all the help and fun.

My deepest and warmest appreciations go to my family, especially my parents for their admirable and endless kindness, love and supportive. I love you so much!

I am so grateful to my brother Vahid for being next to me all these years and being so helpful and kind. Someone to talk to about everything in life and sharing the happy and sad moments! Chakerim! ☺

My true love and appreciation go to my sister Toktam for being a great and extremely caring sister. I shall not forget the help and kindness from Farshid. A big thanks to the little Miss sunshine, Parastoo! You enlighten my life Jooje! ☺

Another big thanks to my wonderful, nice and caring brother Reza and his wife Maryam for their delightful support from far away!

The Swedish Foundation for Strategic Research, the Swedish Research Council, and the Knut and Alice Wallenberg Foundation are acknowledged for financial support.

Bibliography

[1] Y. Makhlin, G. Schön, A. Shnirman, Nanoscale superconducting quantum bits, Physica C **350**, 2001.

[2] M. H. Devoret, A. Wallraff, and J. M. Martinis, Superconducting Qubits: A Short Review, arXiv: cond-mat/0411174v1, 2008.

[3] J. M. Martinis, Superconducting phase qubits, Quantum Inf Process 8:81–103, Springer, 2009.

[4] R.W. Simmonds, K.M. Lang, D.A. Hite, S. Nam, D. P. Pappas, and J. M. Martinis, Decoherence in Josephson Phase Qubits from Junction Resonators, PRL **93**, No.7, 2004.

[5] K. Kakuyanagi, T. Meno, S. Saito, H. Nakano, K. Semba, H. Takayanagi, F. Deppe, and A. Shnirman, Dephasing of a Superconducting Flux Qubit. PRL **98**, 047004, 2007.

[6] T.P. Orlando, K.A. Delin Foundations of applied superconductivity, Addison-Wesley Publishing Company, Inc., 1991.

[7] J. Clarke, SQUIDs: Then and now, International journal of modern physics B, **24**, Nos. 20 & 21, 2010.

[8] J. Clarke, W. M. Goubau, and M. B. Ketchen, Tunnel Junction dc SQUID: Fabrication, Operation, and Performance, Journal of Low Temperature Physics, **25**,1976.

[9] K. M. Lang, D. A. Hite, R. W. Simmonds, R. McDermott, and D. P. Pappas, John M. Martinis, Conducting atomic force microscopy for nanoscale tunnel barrier characterization Review of scientific instruments 75, No.8, 2004.

[10] J.S. Kline, H. Wang, S. Oh, J. M. Martinis and D. P. Pappas, Josephson phase qubit circuit for the evaluation of advanced tunnel barrier materials, Supercond. Sci. Technol. **22**, 2009.

[11] E. Paladino, L. Faoro, G. Falci, and R. Fazio, Decoherence and 1_f Noise in Josephson Qubits, PRL **88**, No. 22, 2002.

[12] Y. Nakamura, Yu. A. Pashkin, and J.S. Tsai, Nature, Coherent control of macroscopic quantum states in a single-Cooper-pair box, Nature **398**, No.29, 1999.

[13] F. C. Wellstood, C. Urbina, and John Clarke, Flicker (1/*f*) noise in the critical

current of Josephson junctions at 0.09–4.2 K, Appl. Phys. Lett., **85**, No. 22, 29, 2004.

[14] F. Yoshihara, K. Harrabi, A. O. Niskanen, Y. Nakamura, and J. S. Tsai, Decoherence of Flux Qubits due to 1/*f Flux* Noise, PRL **97**, 167001, 2006

[15] Radoslaw C. Bialczak, R. McDermott, M. Ansmann, M. Hofheinz, N. Katz, Erik Lucero, Matthew Neeley, A. D. O'Connell, H. Wang, A. N. Cleland, and John M. Martinis, 1/*f* Flux Noise in Josephson Phase Qubits, PRL **99**, 187006, 2007.

[16] S. Oh, K. Cicak, R. McDermott, K.B. Cooper, K.D. Osborn, R.W. Simmonds, M. Steffen, J.M. Martinis and D.P. Pappas, Low-leakage superconducting tunnel junctions with a single-crystal Al_2O_3 barrier, Supercond. Sci. Technol. **18**, 2005.

[17] T. Greibe, M. P.V. Stenberg, C. M. Wilson, T. Bauch, V. S. Shumeiko, and P. Delsing, Are ''Pinholes'' the Cause of Excess Current in Superconducting Tunnel Junctions? A Study of Andreev Current in Highly Resistive Junctions, PRL **106**, 2011

[18] W. H. Rippard, A. C. Perrella, F. J. Albert, and R. A. Buhrman, Ultrathin Aluminum Oxide Tunnel Barriers, PRL **88**, No.4, 2002.

[19] H. Brenning, S. Kubatkin, and P. Delsing, Fabrication of aluminum single-electron transistors with low resistance-capacitance product, Journal of Applied Physics **96**, No.11, 2004.

[20] T. Greibe, T. Bauch, C. Wilson and P. Delsing, Improvement of chip design to reduce resonances in subgap regime of Josephson junctions, Journal of Physics: Conference Series **150**, 2009.

[21] J. Lisenfeld, A. Lukashenko, M. Ansmann, J. M. Martinis, and A.V. Ustinov, Temperature Dependence of Coherent Oscillations in Josephson Phase Qubits, PRL **99**, 170504, 2007.

[22] J. S. Kline, H. Wang, S.Oh, J. M. Martinis, and D. P. Pappas, Josephson phase qubit circuit for the evaluation of advanced tunnel barrier materials, Supercond. Sci. Technol. **22**, 2009.

[23] Kamerling Onnes, H., The Superconductivity of Mercury. Comm. Phys. Lab. Univ. Leiden, **122**: p.124, 1911.

[24] W. Meibner, Ein neuer Effekt bei Eintrirr der Supraleitfähigkeit. Naturwissenschaften, **21**(44): p.787-788, 1933.

[25] T. P. Orlando, K. A. Delin, Foundations of Applied Superconductivity, Addison-Wesley Publishing Company, Inc., 1991.

[26] J. Bardeen, L.N. Cooper, and J.R. Schrieffer, Microscopic Theory of Superconductivity. Physical Review, **106**(1): p. 162-164, 1957.
[27] H. Kroemer, Quantum Mechanics for Engineering, Materials Science, and Applied Physics, Prentice-Hall, Inc., New Jersey, 1994.
[28] B.D Josephson, Possible New Effects in Superconductivity Tunnelling, Physics Letter, **1** (7), 1962.
[29] A. Shnirman, G. Schön, I. Martin, and Y. Makhlin, Low- and High-Frequency Noise from Coherent Two-Level Systems, PRL **94**, 127002, 2005.
[30] T. Lanting, A. J. Berkley, B. Bumble et al. Geometrical dependence of the low-frequency noise in superconducting flux qubits, Phys. Rev. B **79**, 2009.
[31] D. J. Van Harlingen, T. L. Robertson, B. L. T. Plourde, P. A. Reichardt, T. A. Crane, and John Clarke, Decoherence in Josephson-junction qubits due to critical-current fluctuations, Phys. Rev. B **70**, 064517, 2004.
[32] Lara Faoro and Lev B. Ioffe, Microscopic Origin of Low-Frequency Flux Noise in Josephson Circuits, PRL 100, 227005, 2008.
[33] S. Sendelbach, D. Hover, A. Kittel, M. Muck, John M. Martinis, and R. McDermott, Magnetism in SQUIDs at Millikelvin Temperatures, PRL **100**, 2008.
[34] SangKook Choi, Dung-Hai Lee, Steven G. Louie, and John Clarke, Localization of Metal-Induced Gap States at the Metal-Insulator Interface: Origin of Flux Noise in SQUIDs and Superconducting Qubits, PRL 103, 2009.
[35] M. Ohring, Materials science of thin films, second edition, 2002.
[36] W. W. Mullins, The Effect Of Thermal Grooving On Grain Boundary Motion, Acta Metallurgica. **6**,1958.
[37] H. J. Frost, C. V. Thompson, and D. T. Walton, Simulation Of Thin Film Grain Structures-I Grain Growth Stagnation, Acta Metall, Mater. **38**, No.8, 1990.
[38] C. V. Thompson and R. Carel, Stress And Grain Growth In Thin Films, J. Mech. Phys. Solids **44**, No. 5, 1996.
[39] H. J. Frost, C. V. Thompson, and D. T. Walton, Simulation Of Thin Film Grain Structures- II Abnormal Grain Growth, Acta Metall, Mater. **40**, No. 4, 1992.
[40] J. E. Palmer, C. V. Thompson, and Henry I. Smith, Grain growth and grain size distributions in thin germanium films, J. Appl. Phys. **62**, 2492, 1987.
[41] M. Hillert, On The Theory Of Normal And Abnormal Grain Growth, Acta Metallurgica. **13**, 1965.
[42] C. V. Thompson, R. Carel, Texture Development In Polycrystalline Thin Films,

Materials Science and Engineering **B32**, 1995.

[43] O.-P. Saira, A. Kemppinen, V. F. Maisi, and J. P. Pekola, Vanishing Quasiparticle Density In a Hybrid Al/Cu/Al Single-Electron Transistor, Phys. Rev. B **85,** 2012.

[44] J. K. Julin, P. J. Koppinen, and I. J. Maasilta, Reduction Of Low-Frequency 1/*F* Noise In Al–Alo_x–Al Tunnel Junctions By Thermal Annealing, Appl. Phys. Lett. **97**, 2010.

[45] N. A. Court, Quasiparticle Dynamics In A Single Cooper-Pair Transistor, Doctoral Thesis, The University of New South Wales, School of Physics, 2008.

[46] K. K. Yadavallia, A. O. Orlova, G. L. Snidera, and J. Elam, Aluminum Oxide Tunnel Barriers For Single Electron Memory Devices, Microelectronics Journal **36**, 2005.

[47] T. A. Fulton and G. J. Dalan, Observation Of Single-Electron Charging Effects In Small Tunnel Junctions, PRL. **59**, 1987.

[48] M. Gustafsson, Studies Of Acoustic Waves, Noise And Charge Pumping Using Single-Electron Devices, Doctoral Thesis, Chalmers University of Technology, 2012.

[49] P. Krantz, Parametrically pumped superconducting circuits, Licentiate of Engineering Thesis, Chalmers University of Technology, 2013.

[50] K. Bladh, Quantum Coherence in The Single Cooper-pair Box, Doctoral Thesis, Chalmers University of Technology, 2005.

[51] J. I. Goldstein, et al., Scanning Electron Microscopy and X-ray Microanalysis, 3rd Edition, Kluwer Academic/Plenum Publishers, New York, 2003.

[52] P. J. Goodhew, J. Humphreys, and R. Beanland, Electron Microscopy and Analysis, 3rd Edition, Taylor & Francis, NewYork, 2001.

[53] Invitation to the SEM world: JEOL

[54] xP DualBeam System Usr's Guid. 2033, FEI Company: Hillsboro

[55] D.B. Williams and C.B. Carter, Transmission electron microscopy, Springer Science + Business Media, LLC, 1996

[56] J. Börjesson, The Role of Interfacial Microstructure of Perovskite Thin Films - A High Resolution and In Situ Study, Doctoral Thesis, Chalmers University of Technology, 2009.

[57] S. J. Pennycook and D. E. Jesson, High-Resolution Z-Contrast Imaging of Crystals. Ultramicroscopy, **37**(1-4): p. 14-38,1991

[58] M. Haider, S. Uhlemann, E. Schwan, H. Rose, B. Kabius and K. UrbanElectron Microscopy Image Enhanced. Nature, **392**: p. 768–769, 1998

[59] P.E. Batson, N. Dellby and O. L. Krivanek, Sub-ångstrom Resolution Using Aberration Corrected Electron Optics. Nature **418**: p. 617-620, 2002

[60] J. Angseryd, Microstructure of a Cubic Boron Nitride Tool Material and its Degradation During Hard Turning Operations, Doctoral Thesis, Chalmers University of Technology, 2011.

[61] Gatan, Gatan Electron Microscopy School-EELS Imaging an Analysis, Pleasanton, 2008.

[62] Egerton, R.F., Electron Energy-Loss Spectroscopy in the Electron Microscope. 2nd Edithion, Plenum Press, New York, 1996.

[63] Brydson, R., Electron Energy Loss Spectroscopy, Taylor & Francis, New York, 2001.

[64] R. M. Langford and A. K. Petford-Long, Preparation Of Transmission Electron Microscopy Cross-Section Specimens Using Focused Ion Beam Milling, J. Vac. Sci. Technol. A **19**, 2186, 2001.

[65] S. Bals, W. Tirry, R. Geurts, , Z. Yang, and D. Schryvers, High-Quality Sample Preparation By Low Kv Fib Thinning For Analytical Tem Measurements. Microsc Microanal **13**, 80–86, 2007.

[66] L. A. Giannuzzi and F. A. Stevie, A Review Of Focused Ion Beam Milling Techniques For TEM Specimen Preparation. Micron **30**, 197–204, 1999.

[67] J. Y. Dai, S. F. Tee, C. L. Tay, Z. G. Song, S. Ansari, E. Er, and S. Redkar, Development Of A Rapid And Automated TEM Sample Preparation Method In Semiconductor Failure Analysis And The Study Of The Relevant TEM Artifact, Microelec. J. **32**, 221–226, 2001.

[68] P. Lawrence, The Dualbeam (FIB/SEM) and its applications - Nanoscale sample preparation and modification, Singapore: PTE Ltd Pacific Tech Centre, 2006.

[69] H. Pettersson, S. Nik, J. Weidow, and E. Olsson, A Method for Producing Site-Specific TEM Specimens from Low Contrast Materials with Nanometer Precision, Microsc. Microanal. **19**, 73–78, 2013.

[70] T. Lilijefors, PhD Thesis, Chalmers University of Technology, 2007.

[71] Fischione 1010 Ar ion mill, Manual.

Appendix A

Fabrication recipe: $Al/AlO_x/Al$ Josephson junctions for TEM characterization

Philip Krantz [1]
[1] Department of Microtechnology and Nanoscience (MC2), Chalmers University of Technology, SE - 412 96, G¨oteborg, Sweden

E-mail: philip.krantz@chalmers.se

Notes:
This recipe was used when gold pads were introduced for normal state resistance measurements of the Josephson junctions. In the cases of fabrication of trilayer samples and Josephson junctions without gold contacts the photolithography step was left out.

1. Cleaning the wafer

1165 Remover, <70 °C, 10 min
Ultrasonic bath, 1 min, circulation
Quick dump rinse bath, DI-water
Rinse in isopropanol (IPA) Blowdry
with N_2

2. Photolithography to define alignment marks and probe pads

Ashing in O_2-plasma, 10 s, 50 W Pre-bake, 1 min, 110 °C
Spin LOR3B, 3000 rpm, 1 min, tacc = 1.5s(≈350nm)
Softbake 5 min, 200 °C Spin S1813, 3000 rpm, 1 min, tacc
= 1.5s(≈150nm) Softbake 2 min, 110 °C Expose, MA6 mask
aligner: 6 W/cm^2, texp = 8.5 s, Lo-vac mode Develop,
MF319, 45 s (Lift up and rinse after 20 s.)

3. E-beam evaporation of alignment marks and contact pads

Ashing in O_2-plasma, 20 s, 50 W Electron beam evaporation, (Lesker PVD225), $P_{ch} \leq 10^{-7}$ mbar Sticking layer: Ti, 30 ˚A/s A, 1 ˚Contact layer: Au, 800 ˚A/s A, 2 ˚Stopping layer: Pd, 100 ˚A/s A, 1 ˚Lift-off excess metals, 1165 Remover, <70 °C, ≈ 50 min Rinse in IPA Blowdry with N_2

4. Semi-dicing of wafer

Spin protective resist, S1813, 2000 rpm, 1 min Softbake, 2 min, 130 °C Dice wafer from backside, leaving 150 µm of the wafer Remove protective resist: 1165 Remover, <70 °C, 10 min Rinse in IPA Blowdry with N_2

5. Electron beam lithography to define Josephson junctions

Ashing in O_2-plasma, 20s 50W Spin Nano Copolymer in Ethyl Lactate 10%, 500 rpm, t_{acc} = 2 s for 5 s, spin 2000 rpm, t_{acc} =0, 5 s for 45 s (≈ 570 nm) Softbake 5 min, 170 °C Spin ZEP 520A 1:1 Anisole, 3000 rpm, t_{acc} =1.5 s, spin 1 min (≈150 nm) Softbake 5 min, 170 °C Spin Espacer 300Z (Electrification dissipating), 2000 rpm, t_{acc} = 1 s, spin 1 min Softbake 1 min, 90 °C Expose, JEOL JBX-9300FS 2nA, 100kV, dose 150 µC/cm^2, Proximity corrected into 16 layers Dice wafer into individual samples, 50µm thick blade Develop top layer of ZEP 520A, O-xylene, 2 min Dip in isopropyl alcohol (IPA) Develop bottom layer Nano Copolymer H_2O:IPA 1:4, 4 min 50 s (undercut ≥ 0.2µm)

6. Two-angle evaporation of Josephson junctions[1]

Ashing in O_2-plasma, 10 s, 50 W Electron beam evaporation in the Plassys: Bottom layer: 15 nm, Rate: 5 /s, α = 28° Dynamic oxidation, Pox = 0, 2 mbar, tox = 10 min Evaporate top electrode, 60 nm, Rate: 5 /s, α = −28° Lift-off excess Al, 1165 Remover, <70 °C, ≈20 min Rinse in IPA and blowdry with N_2-gun

[1] This is an example of parameters used. For different samples, the evaporation angles, layer thicknesses, and oxidation parameters varied.